An approach to quantify depth-resolved marine photochemical fluxes using remote sensing: Application to carbon monoxide (CO) photoproduction

Cédric G. Fichot [a,b,*], William L. Miller [a]

[a] Department of Marine Sciences, University of Georgia, Athens, GA 30605, USA
[b] Department of Marine Sciences, University of South Carolina, Columbia, SC 29208, USA

ABSTRACT

This paper presents a model to calculate depth-resolved marine photochemical fluxes from remotely sensed ocean color and modeled solar irradiance. The basic approach uses three components: 1) below-sea-surface spectral downward scalar irradiance calculated from a radiative transfer model (STAR) and corrected for clouds using TOMS UV reflectivities; 2) surface-ocean spectral diffuse attenuation coefficients and absorption coefficients for chromophoric dissolved organic matter retrieved from SeaWiFS ocean color using the SeaUV/ SeaUVc algorithms; and (3) spectral apparent quantum yield for the photochemical reaction considered. The output of the model is a photochemical rate profile, $\Psi_{PR}(z)$, where z represents depth.

We implemented the model for carbon monoxide (CO) photochemistry using an average apparent quantum yield spectrum and generated a monthly climatology of depth-resolved CO photoproduction rates in the global ocean. The climatology was used to compute global budgets and investigate the spatial and seasonal variabilities of CO photoproduction in the ocean. The model predicts a global CO photoproduction rate of about 41 TgC yr^{-1}, in good agreement with other recent published estimates ranging from 30 to 84 TgC yr^{-1}. The fate of photochemically derived CO and its role in global biogeochemical cycles remains uncertain however, with biological consumption and sea–air exchange competing for its removal in the surface ocean. Knowledge of the vertical distribution of CO photoproduction is critical in the quantification of the relative magnitudes of these sink mechanisms. The depth-resolution capabilities of this model, together with US Naval Research Laboratory climatology for mixed layer depths allowed further estimation that >95% of the total water-column CO photoproduction occurs within the mixed layer on a global, yearly basis. Despite this compelling figure, the model also suggests significant spatio-temporal variability in the vertical distribution of CO photoproduction in the subtropical gyres, where up to 40% of water-column CO can be produced below the mixed layer during summertime.

While the approach can be applied to other photochemical fluxes (e.g. DIC formation or DMS removal), accurate quantification of such processes with remote sensing will be limited until the mechanisms regulating observed oceanic variability in the apparent quantum yields are better understood. Minor modification to this model can also make it applicable for the determination of the effects of UV and visible solar radiation on sensitive biological systems.

1. Introduction

Major uncertainties currently exist within global budgets of carbon, nitrogen, phosphorous and sulfur (Berner & Lasaga, 1989; IPCC, 2001; Sarmiento, 1993). Attempts at filling gaps in these budgets have led scientists to recognize the potential role of marine photochemistry in global biogeochemical cycling. In its broadest

sense, marine photochemistry refers to the chemical processes that result from the interaction of solar radiation with all seawater constituents. However, since most photochemically efficient solar radiation (ultraviolet and blue region of the solar spectrum, 280–500 nm) in the ocean is scavenged by chromophoric dissolved organic matter (CDOM), most marine photochemical studies deal with the effects of solar radiation on the dissolved constituents of seawater.

Studies over the past four decades have demonstrated that marine photochemistry is involved in a variety of chemical reactions of significance to numerous marine, atmospheric and climate-related processes (Mopper & Kieber, 2000; Zepp et al., 1998, 2007). Through absorption of solar radiation, the ubiquitous CDOM undergoes

* Corresponding author. Department of Marine Sciences, University of Georgia, Athens, GA 30605, USA.
  E-mail address: cgfichot@gmail.com (C.G. Fichot).

photochemical reactions, serving as the major precursor for the creation of a variety of short-lived radicals and stable photoproducts. Photoproducts important to carbon cycles include dissolved inorganic carbon (DIC: CO_2, HCO_3^-, CO_3^{2-}), carbon monoxide (CO) and a variety of low molecular weight (LMW) biologically labile carbon compounds (Mopper & Kieber, 2001). Among other processes, marine photochemistry also acts as: a direct sink for dissolved organic matter (DOM); a source of volatile sulfur compounds (COS and CS_2) (Uher & Andreae, 1997; Xie et al., 1998) and methyl iodide (CH_3I) (Moore & Zafiriou, 1994); a potentially significant and indirect sink for dimethyl sulfide (DMS) in the ocean (Brimblecombe & Shooter, 1986; Kieber et al., 1996).

In light of these recent findings, the need to quantify the role of marine photochemical processes in global biogeochemical cycles is being increasingly recognized by the scientific community. The quantitative assessment of these processes, however, has been severely hindered by the lack of a robust extrapolation scheme to apply experimental results to the seasonal and regional-scale calculation of photochemical fluxes. Fortunately, quantification of marine photochemical processes is amenable to remote sensing because of its critical dependence on ocean UV and visible optical properties. In the present work, we exploit this property by developing and implementing a model for the calculation of depth-resolved photoprochemical fluxes on a global scale using remote sensing data. Our model uses the high spatial and temporal coverage offered by the ocean color Sea-viewing Wide Field-of-view Sensor (SeaWiFS) and the Total Ozone Mapping Spectrometer (TOMS).

The purpose of this work is to improve the quantification of photochemically-driven processes in the global ocean and is a continuation of earlier work by Cullen et al. (1997), Johannessen (2000), Fichot (2004) and Fichot et al. (2008). Our approach presents the significant advantage of quantifying *depth-resolved* rates, thus providing the depth distribution of photochemical fluxes. Knowledge of this depth distribution is critical when evaluating the relative contribution of other depth-sensitive processes (e.g. air–sea gas exchange) affecting the *in situ* concentration of photoproducts. In that sense our approach distinguishes itself from the method of Bélanger et al. (2006) used to quantify depth-integrated photomineralization rates of terrigenous dissolved organic matter in Arctic coastal waters.

In this study we implement our model exclusively for the calculation of depth-resolved photoproduction rates of CO. Carbon monoxide was chosen as a study species amid other marine photoproducts (e.g. H_2O_2, CO_2, and COS) for several reasons. First, and most importantly, CO is well-studied with regard to its natural variability in the apparent quantum yield, discussed in greater detail later in this paper. Second, marine photochemistry can be considered as the major source of carbon monoxide in the surface ocean (Conrad et al., 1982; Jones, 1991; Seiler & Junge, 1970; Swinnerton et al., 1970), although dark (e.g. thermal) production has been recognized recently as a potentially important source of CO in the global ocean (Zhang et al., 2008). While some species of marine algae and bacteria are known to produce CO, they are minor contributors in the global ocean relative to marine photochemistry (Jones & Morita, 1983; Loewus & Delwiche, 1966). Third, CO photoproduction represents a potentially important pathway of remineralization of oceanic DOC with rates greater than the sum of all identified LMW carbon-containing photoproducts (based on carbon mass), with the exception of CO_2 (Kieber et al., 1989; Miller & Zepp, 1995; Mopper & Kieber, 2001; Mopper et al., 1991). Finally, the relative magnitude of CO removal mechanisms in the ocean (e.g. microbial consumption and venting to the atmosphere) depends heavily on its depth of production. The estimation of *depth-resolved* rates thus represents an important tool in assessing the role of photochemically produced CO in global biogeochemical cycles.

2. Methods

2.1. Photochemical rate model

Our model is designed to estimate photochemical rates in the ocean that result solely from the interaction of solar radiation with the dissolved constituents of seawater. Its description is separated in two parts. First, we describe the general, ideal model that should be used to quantify depth-resolved CO photoproduction rates. Second, we outline a practical model derived from the general model that can be practically applied to photochemical calculations on a global scale using remotely sensed data.

2.1.1. General model

The absorption of a photon (photoexcitation) is the first and fundamental step in any photochemical process. Therefore, the rate of photons absorbed by CDOM needs to be quantified as a function of depth in order to calculate depth-resolved photochemical rates.

The product of spectral scalar irradiance, $E_o(\lambda, z)$ (mol(photons) m^{-2} s^{-1} nm^{-1}), and CDOM absorption coefficient, $a_g(\lambda, z)$ (m^{-1}), is used to quantify the photon absorption rate (by CDOM) for a given wavelength and a given depth, where λ (nm) and z (m) refer to the wavelength and depth throughout this manuscript. In turn, $E_o(\lambda, z)$ can be expressed in terms of the spectral scalar irradiance just below the surface, $E_o(\lambda, 0^-)$, and the average diffuse attenuation coefficient of scalar irradiance for the $0-z$ depth range, $K_o(\lambda)$ (m^{-1}), as shown in Eq. (1),

$$E_o(\lambda, z) = E_o(\lambda, 0^-)e^{-K_o(\lambda)z}, \tag{1}$$

so that the photon absorption rate, $\Xi(\lambda, z)$ (mol(photons)m^{-3} $s^{-1}nm^{-1}$), can be expressed as in Eq. (2),

$$\Xi(\lambda, z) = E_o(\lambda, 0^-)e^{-K_o(\lambda)z}a_g(\lambda, z). \tag{2}$$

Once a photon is absorbed by CDOM, the subsequent dissipation of energy occurs through a variety of photophysical and photochemical pathways, yielding either heat or radiation along with an unchanged molecule (e.g. vibrational/rotational energy, internal conversion, collisional deactivation, and fluorescence). Only a small portion of absorbed energy results in reactions with acceptor molecules in solution (e.g. ground state triplet molecular oxygen, metals, etc…) and/or primary photochemical reactions (e.g. molecular rearrangement, fragmentation or reaction with metal ions or molecular oxygen) (Miller, 1994).

The probability that an absorbed photon leads to a specific photochemical reaction is typically small and depends on the energy (and therefore the wavelength) of the photon absorbed. CO photoproduction is therefore dependent on the wavelength-specific efficiency with which an absorbed photon generates a photochemical reaction yielding CO. This efficiency is generally described in terms of the apparent quantum yield (AQY), $\phi_{CO}(\lambda)$ (mol(CO) mol(photons)$^{-1}$), calculated as the ratio of moles of photoproduct formed to the moles of photons of wavelength λ absorbed. The term "apparent" is necessary because the structures of the particular chromophores within the CDOM are not well characterized. Consequently, the absorption of the entire CDOM pool must be used in AQY calculations, instead of the absorption of specific chromophores or reaction centers specific to each photoproduct of interest.

The rate of CO photoproduction at depth z attributable to the absorption of photons of wavelength λ can be computed as the product of $\Xi(\lambda, z)$ and $\phi_{CO}(\lambda, z)$ as in Eq. (3):

$$\Psi_{CO}(\lambda, z) = \frac{d[CO]}{dt}(\lambda, z) = \Xi(\lambda, z)\phi_{CO}(\lambda, z), \tag{3}$$

where $\Psi_{CO}(\lambda, z)$ is the CO photoproduction rate at depth z (mol(CO) $m^{-3} s^{-1} nm^{-1}$). A schematic illustrating the concept and variables used in the quantification of $\Psi_{CO}(\lambda, z)$ is displayed in Fig. 1. Integrating $\Psi_{CO}(\lambda, z)$ over the entire spectrum of photochemically-active solar radiation ($\lambda_{min} - \lambda_{max}$) represents a proper formulation of the photo-production rate of CO at depth z (mol(CO) $m^{-3} s^{-1}$), as shown in Eq. (4):

$$\Psi_{CO}(z) = \int_{\lambda_{min}}^{\lambda_{max}} E_o(\lambda, 0^-) e^{-K_o(\lambda)z} a_g(\lambda, z) \phi_{CO}(\lambda, z) d\lambda. \tag{4}$$

2.1.2. Practical model

Only a simplified model can be realistically implemented when using remotely sensed data. A few reasonable assumptions can be made to simplify model 4 for the application to modeling of photochemical rates.

First, considering the spectral characteristics of the incident irradiance and those of the AQY of CO, it is reasonable to reduce the spectral window of integration. Absorption of solar radiation by stratospheric ozone and increased scattering at low wavelengths result in a flux of photons at wavelength <290 nm that accounts for an insignificant portion of the total photoproduction. At longer wavelengths, both $a_g(\lambda)$ and $\phi_{CO}(\lambda)$ decrease exponentially with increasing wavelength, resulting in incident photons of wavelength $\lambda > 490$ nm being both minimally absorbed and lacking the energy required to produce a molecule of CO (Blough & Del Vecchio, 2001; Mopper & Kieber, 2001; Nelson & Siegel, 2001; Zafiriou et al., 2003). Assuming that photons of wavelength $\lambda > 490$ nm account for a very small portion of the total photoproduction and that photons of $\lambda < 290$ nm are exceedingly scarce at the earth's surface, our integrations for CO photoproduction only include wavelengths from $\lambda = 290$ to 490 nm. We tested the model with a representative range of inputs and estimated that this assumption resulted in an error of less than 1% in the estimated rates relative to a model run with the 280–700 nm spectral window of integration.

Second, total scalar irradiance incident to the CDOM at a particular depth z can be separated into a downwelling and an upwelling component, $E_{od}(\lambda, z)$ and $E_{ou}(\lambda, z)$, respectively, where $E_o(\lambda, z) = E_{od}(\lambda, z) + E_{ou}(\lambda, z)$ (Kirk, 1994). The contribution of upwelling scalar irradiance varies in a complex manner with the incident light field and the inherent optical properties of the water (Kirk, 1989; Mobley, 1994). In shallow regions with reflective sediments, significant UV radiation can end up traveling in the upward direction. Modeling studies and field measurements, however, have shown that the proportion of upwelling irradiance is generally very small (a few percent) compared to the total scalar irradiance so that $E_{ou}(\lambda) \ll E_{od}(\lambda)$ (Kirk, 1994). For the purpose of our study, it is therefore reasonable to assume that $E_{od}(\lambda, z) \simeq E_o(\lambda, z)$. Although it may not always be negligible (e.g. where sediment concentration is high), ignoring $E_{ou}(\lambda)$ is expected to add only a small error to our photochemical prediction while removing complexity from the model.

Third, the attenuation of downwelling *scalar* irradiance as a function of depth can be approximated using an average diffuse attenuation coefficient for downwelling irradiance, $K_d(\lambda)$. Kirk (1994) demonstrates that for most natural waters $K_d(\lambda)$ is very close in value to that of $K_o(\lambda)$
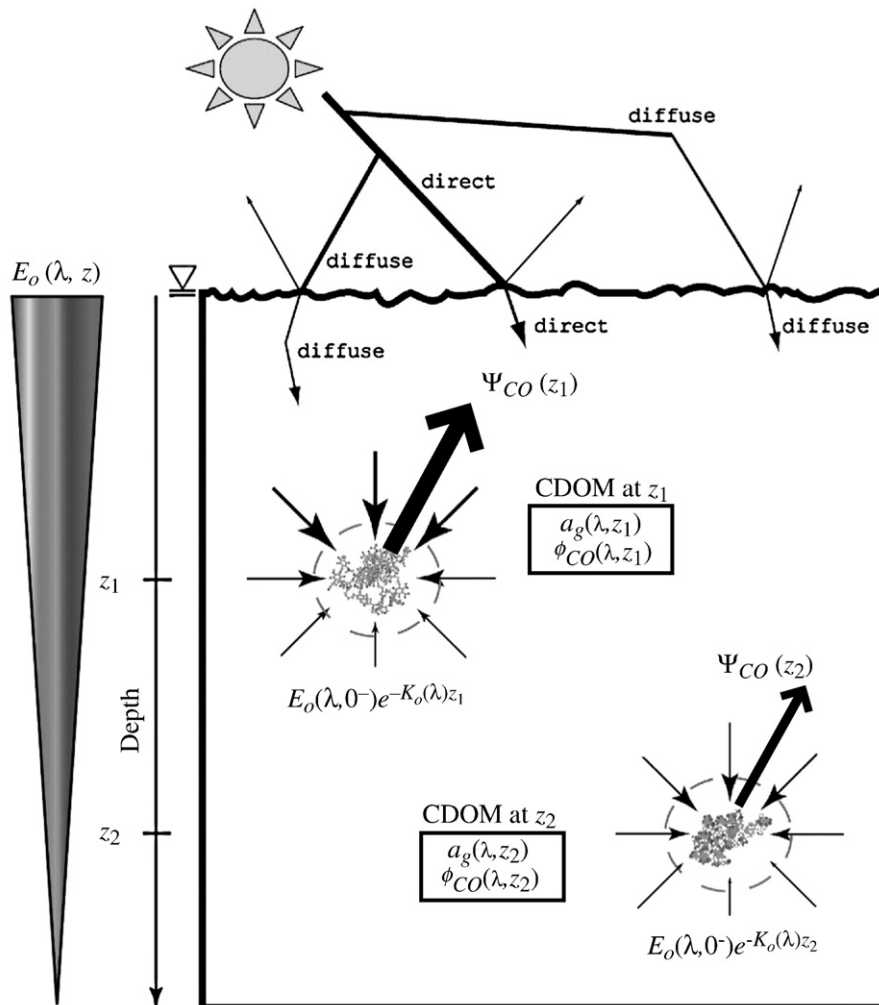

Fig. 1. Variables involved in the quantification of depth-resolved photoproduction rates using the general model.

(within a few percent). Here, we estimate the downwelling scalar irradiance at depth z, $E_{od}(\lambda, z)$, from the downwelling scalar irradiance just below the surface $E_{od}(\lambda, 0^-)$ by using an average $K_d(\lambda)$ for the $0 - z$ m depth range.

These three assumptions are used to convert the complex model (Eq. (4)) to a simpler photochemical model that is more tractable for global scale calculations, shown in Eq. (5):

$$\Psi_{CO}(z) \simeq \int_{290}^{490} E_{od}(\lambda, 0^-) e^{-(K_d(\lambda)z)} a_g(\lambda, z) \phi_{CO}(\lambda, z) d\lambda. \qquad (5)$$

2.2. Data and implementation

The practical model was used to calculate profiles of daily-integrated photoproduction rates at mid-month conditions for each month of the year. Daily-integrated $\Psi_{CO}(z)$ are referred to as $\Psi_{CO}^{Day}(z)$ (mol(CO) m^{-3} day^{-1}) throughout the paper. By integrating rates over 24 h we assume that $K_d(\lambda)$, $a_g(\lambda)$ and $\phi_{CO}(\lambda)$ are constant over the course of a day. The calculation of CO photoproduction profiles also implies that these same variables are averages for the water column, and accordingly, do not vary with depth. Under these assumptions, we rewrite Eq. (5) as follows:

$$\Psi_{CO}^{Day}(z) \simeq \int_{290}^{490} E_{od}^{Day}(\lambda, 0^-) e^{-(K_d(\lambda)z)} a_g(\lambda) \phi_{CO}(\lambda) d\lambda \qquad (6)$$

where $E_{od}^{Day}(\lambda, 0^-)$ (mol(CO) m^{-3} day^{-1}) refers to the daily-integrated, cloud-corrected downwelling scalar irradiance. Spectra of $E_{od}^{Day}(\lambda, 0^-)$, $K_d(\lambda)$, $a_g(\lambda)$, $\phi_{CO}(\lambda)$ and spectra of the corresponding photochemical responses, $\Psi_{CO}^{Day}(\lambda, z)$ (mol(CO) m^{-3} day^{-1} nm^{-1}), at

$z = 0^-$, 1 and 5 m, are shown in Fig. 2 at a representative station in the South Atlantic Bight of the United States for mid-April conditions (station 2 in Fig. 6).

Because of computational limitations, we chose a spectral resolution of 5 nm and the following vertical resolution: 0.1 m for $z < 10$ m; 0.2 m for $10 \leq z < 20$ m; 0.5 m for $20 \leq z < 50$ m; 1 m for $50 \leq z < 100$ m; 5 m for $100 \leq z < 200$ m; 20 m for $200 \leq z < 500$ m and 50 m for $z > 500$ m. The vertical resolution of the model is set to be finer near the surface than at depth because photoproduction decreases exponentially with depth. We tested the model with a representative range of inputs and estimated that these spectral and vertical resolutions resulted in a minimal uncertainty of <4% (<1% and 3%, respectively) relative to a 1-nm spectral resolution and a constant vertical resolution of 0.01 m.

Our assumption that $K_d(\lambda)$, $a_g(\lambda)$ and $\phi_{CO}(\lambda)$ are homogenous throughout the water column is an important consideration that results from the limitations of remote sensing techniques in providing depth-resolved information. The optical properties estimated from remotely sensed ocean color are typically representative of the first optical depth of the ocean (surface layer of the ocean extending from just below the surface to depth z_{1od}, where $E_d(z_{1od})$ has reached $1/e$ of its below-surface value) (Gordon & McCluney, 1975). As a result, the retrievals made using this approach are typically average values for the first optical depth. While this assumption should work well for this layer, actual rates below it may differ significantly from our estimates. We further discuss the uncertainty associated with this assumption in Section 3.3.

In the rest of Section 2.2, we describe the retrieval and implementation of the four variables used in the photoproduction model
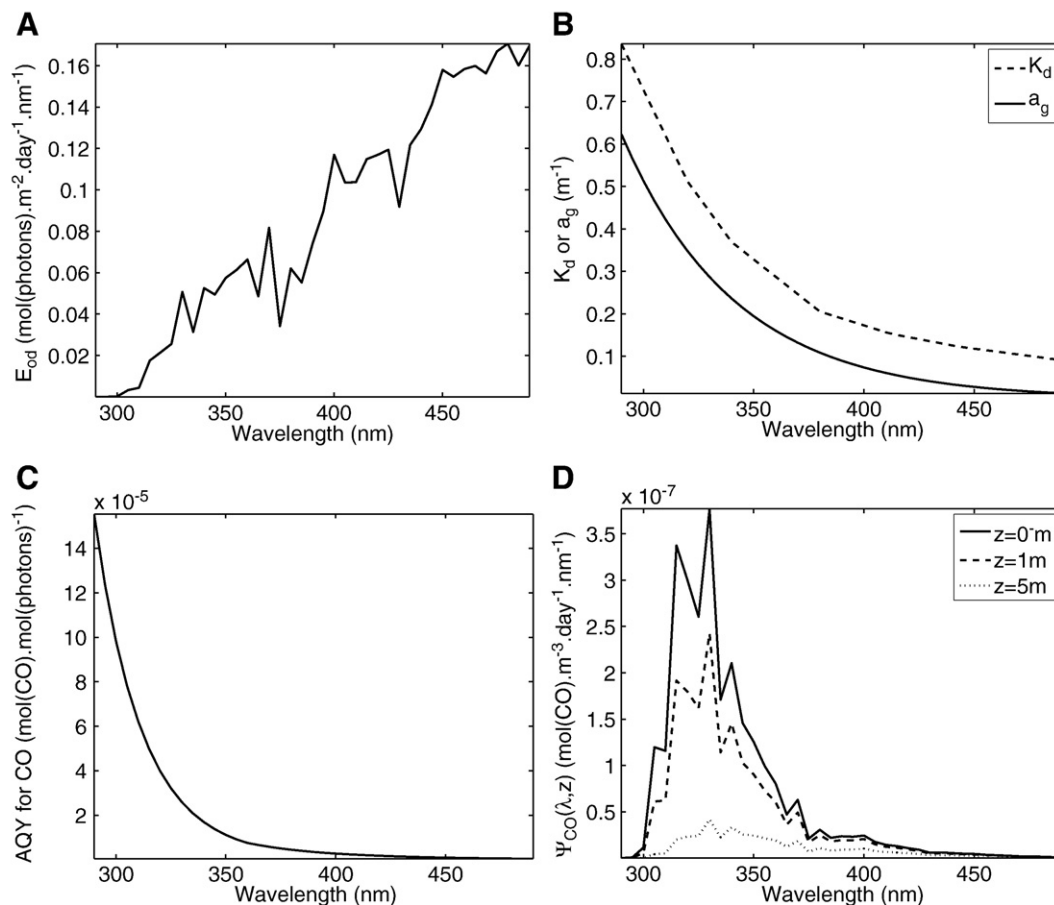

Fig. 2. Spectra of the modeled/published variables used in the calculation of the depth-resolved photoproduction rates and photochemical production spectral response at 0^- m, 1 m, and 5 m for a specific location (30.78°N/80.46°W, South Atlantic Bight, April: see Station 2 in Fig. 6).

described in Eq. (6). We review the sensitivity of the model outputs to uncertainties in these variables in Section 3.3.

2.2.1. $E_{od}^{Day}(\lambda, 0^-)$

We used the System for Transfer of Atmospheric Radiation (STAR) to model clear-sky, global (= direct + diffuse fractions) downwelling irradiance spectra reaching the air–sea interface, $E_d^{cs}(\lambda, 0^+)$, at every nanometer in the $\lambda = 280$–700 nm spectral range. Developed at the Meteorological Institute at the University of Munich, STAR is a radiative transfer model based on the work of Ruggaber et al. (1994). The UNIX STARsci version of the STAR model was used in this study. Monthly zonal (latitudinal) average total ozone concentrations from the Total Ozone Mapping Spectrometer (TOMS) were used as inputs to STAR. Other inputs to the model were chosen appropriately according to the season and latitude concerned (e.g. humidity profile and ozone profile). Based on values generally observed for the ocean (Remer et al., 2005), a constant aerosol optical thickness $\tau_a = 0.1$ at 550 nm was used in the model assuming "clean maritime" aerosols, while SO_2 and NO_2 gas concentrations were ignored as STAR model inputs. This unconstrained variability in aerosol optical properties is expected to represent a source of uncertainty of a few percents in our modeled irradiances (Jin et al., 2002).

$E_d^{cs}(\lambda, 0^+)$ was generated for every hour of the day (0–24 h), at every 10° latitude from 90°N to 90°S and for the 15th day of every month of the year. Effects of clouds, reflection at the air–sea interface under the assumption of a flat ocean, conversion to scalar downwelling irradiance and integration over time (24 h) were all accounted for in the conversion of modeled $E_d^{cs}(\lambda, 0^+)$ to cloud-corrected, daily-integrated, downwelling scalar irradiance, $E_{od}^{Day}(\lambda, 0^-)$. The correction for clouds makes use of TOMS UV reflectivities collected from 1996 to 2003 and compiled into monthly climatologies. The details of the conversion from $E_d^{cs}(\lambda, 0^+)$ to $E_{od}^{Day}(\lambda, 0^-)$ are given in Appendix A. Global maps of $E_{od}^{Day}(\lambda, 0^-)$ at $\lambda = 320$ nm modeled for January 15th, April 15th and July 15th are displayed in Figs. 3A, C and E, respectively.

A comparison of several atmospheric radiative transfer models and *in situ* radiometric measurements concluded that under clear-sky conditions, STAR estimates solar spectral irradiances accurately, particularly in the UV region (Neale et al., 2001). Despite these encouraging results, a proper validation of our approach (deriving $E_{od}^{Day}(\lambda, 0^-)$ from STAR outputs) represents a formidable task involving the long-term deployment of radiometers at multiple
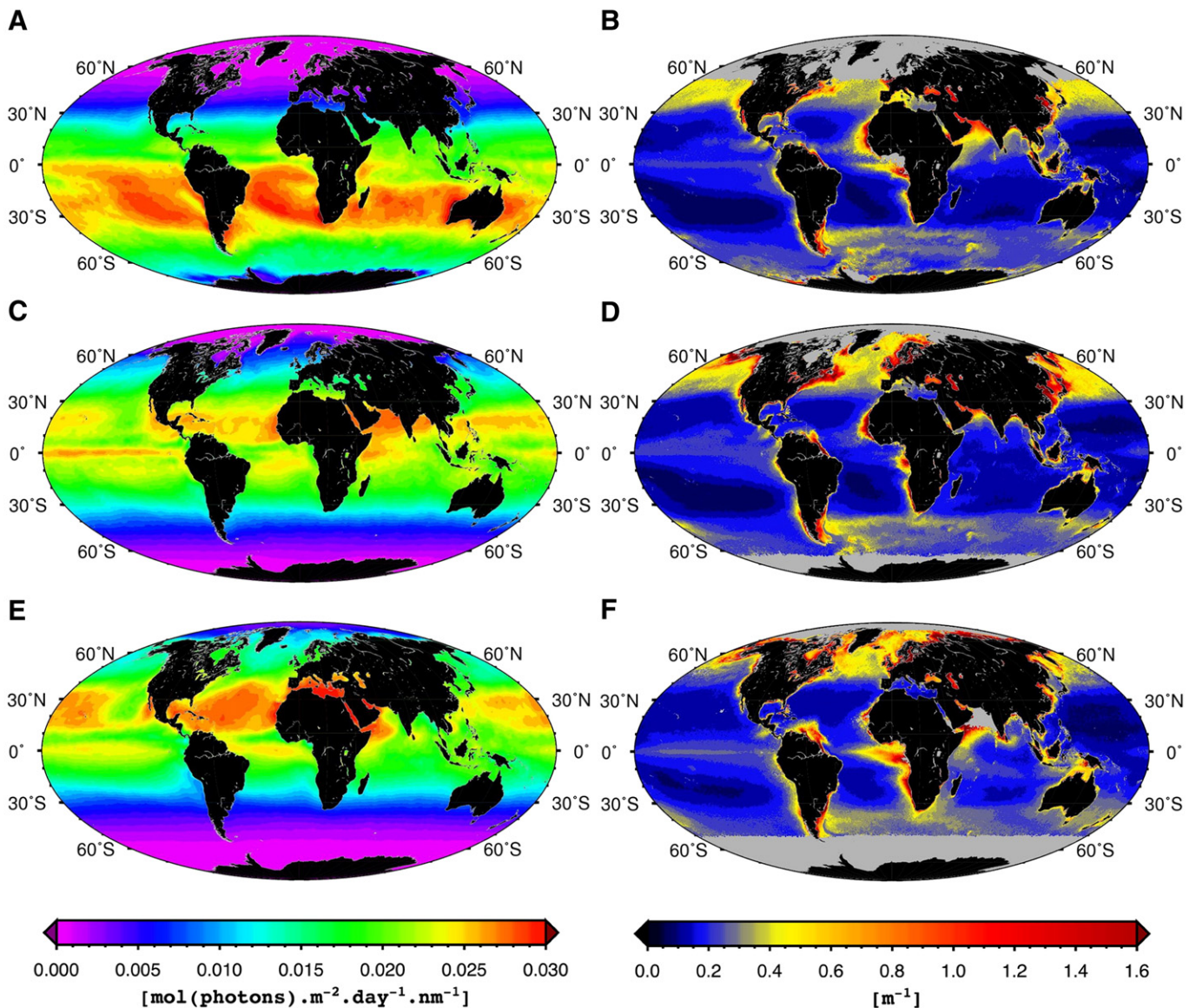

Fig. 3. Global maps of $E_{od}^{Day}(320, 0^-)$ and $K_d(320)$ used as inputs to the model in Eq. (3) for the calculation of the depth-resolved photoproduction rates (left and right columns, respectively). Three different months are displayed: January (A,B), April (C,D) and July (E,F). Regions in gray represent areas where SeaWiFS ocean color are unavailable.

locations. We are currently proceeding with the partial validation of this approach using several 12-day long, ship-based deployments of multispectral Satlantic® radiometers (305–683 nm range) in the Gulf of Mexico. At this stage, we are therefore forced to assume that ±30% is a reasonable uncertainty in $E_{od}^{Day}(\lambda, 0^-)$ for the sensitivity analysis. The reader should keep in mind, however, that this uncertainty can be significantly different from ±30%.

2.2.2. $K_d(\lambda)$

The Sea*UV* algorithm (Fichot et al., 2008) was implemented to SeaWiFS normalized water-leaving radiances, $nLw(\lambda)$, in order to retrieve diffuse attenuation coefficients, $K_d(\lambda)$, at $\lambda = 320, 340, 380, 412, 443$ and 490 nm. Monthly-binned normalized water-leaving radiances collected continuously by SeaWiFS from September 16, 1997 until August 31, 2007 (10 years) were used to calculate monthly climatologies for the entire ocean with a spatial resolution of $40 \times 40 \cos(\phi)$ km, where ϕ is the latitude (grid size of 500×1000 pixels). In some situations (mostly at high latitudes), atmospheric interference or lack of incident radiation makes the remote sensing of accurate reflectances impossible and consequently these data were not included in our analysis. On a pixel basis, any data with a value three standard deviations higher or lower than the 10-year mean were excluded from the climatology.

Full spectra of $K_d(\lambda)$ in the $\lambda = 320–490$ nm wavelength range are obtained from a cubic interpolation between bands. Using $K_d(320)$ and $K_d(340)$, we calculate a spectral slope coefficient $S_{Kd} = (\ln[K_d(320)] - \ln[K_d(340)])/(320 - 340)$ that describes the spectral variations of $K_d(\lambda)$ between 320 and 340 nm. This coefficient is used to extrapolate $K_d(\lambda)$ in the $\lambda = 290–319$ nm range using the relationship $K_d(\lambda) = K_d(320)e^{(-S_{Kd}(\lambda - 320))}$. The validation of SeaUV with both modeled Hydrolight and measured *in situ* data sets shows that $K_d(\lambda)$ is estimated with an uncertainty of ±15–20%, depending on the wavelength considered (Fichot et al., 2008). However, a solid match-up analysis between remotely sensed and measured *in situ* $K_d(\lambda)$ remains a difficult task due to the relative scarcity of *in situ* $K_d(\lambda)$ measurements in the UV. We therefore consider ±30% to be a reasonable uncertainty for $K_d(\lambda)$ retrieved from SeaWiFS ocean color using SeaUV.

Monthly climatologies of $K_d(\lambda)$ estimated at $\lambda = 320$ nm for January, April and July are displayed on global maps in Figs. 3B, D and F, respectively. Note that $K_d(\lambda)$ retrieved using SeaUV is typically representative of low solar zenith angle (<45%) and that we ignore the dependency of $K_d(\lambda)$ on solar zenith angle when calculating daily-integrated photoproduction rates. However, the resulting uncertainty in daily-integrated rates is expected to be very small, as a result of the combination of two factors: 1) $K_d(\lambda)$ is weakly dependent on solar zenith angle for $\lambda < 490$ nm and should be weakest in the UV region (Zheng et al., 2002); 2) the maximum error would occur at high solar zenith angles when photochemical rates are low and contribute to a small fraction of the daily-integrated rate. In the error analysis, we consider this error as embedded in the ±30% uncertainty in $K_d(\lambda)$ estimated from ocean color.

2.2.3. $a_g(\lambda)$

The absorption coefficient of CDOM at $\lambda = 320$ nm, $a_g(320)$, is estimated from $K_d(320)$ by assuming a constant ratio $a_g(320)/K_d(320) = 0.68$. At other wavelengths ($\lambda = 290–490$ nm), $a_g(\lambda)$ was estimated assuming an exponential spectrum: $a_g(\lambda) = a_g(320)e^{(-S_{ag}(\lambda - 320))}$, where $S_{ag} = 0.0194$.

The ratio $a_g(320)/K_d(320)$ was estimated from an extensive set of simultaneous *in situ* measurements (123 measurements) of $a_g(\lambda)$ ($\lambda = 290 - 700$ nm) and $K_d(\lambda)$ ($\lambda = 320, 340, 380, 412, 443$ and 490 nm). The coefficient S_{ag} was estimated from the same $a_g(\lambda)$ spectra using a non-linear fit over the 290–400 nm region. The data were collected within a reasonable time window around solar noon (in order to preserve the quasi-inherency of $K_d(\lambda)$) and in a variety of marine environments which include: the coastal and open waters of the Middle

Atlantic Bight, the oligotrophic waters of the Loop Current in the Gulf of Mexico, the CDOM-rich waters of the Bay of Florida, the productive waters of the Santa Barbara channel (during different seasons), the waters west of the Antarctic Peninsula (during different seasons) and the open waters of the North Pacific Ocean before and after and iron-enrichment experiment (Canadian SOLAS project, summer 2002). CDOM is the main contributor to UV attenuation in most marine waters and the ratio was more constant at $\lambda = 320$ nm (0.68 ± 0.13) than at longer wavelengths. More details regarding the regions sampled can be found in Fichot (2004) and Fichot et al. (2008).

The uncertainty associated with retrieving $a_g(\lambda)$ from SeaWiFS ocean color was estimated from a match-up analysis between remotely sensed $a_g(400)$ and simultaneous, independent, *in situ* measurements. The analysis included 217 match-ups for various areas of the world's ocean (California coast, Gulf of Mexico, Gulf of Maine, Middle Atlantic Bight, Labrador Sea, Eastern North Atlantic, Central Atlantic Ocean, Sea of Japan, Indian Ocean, and Southern Ocean). The *in situ* $a_g(\lambda)$ spectra were obtained by querying the SeaWiFS Bio-optical Archive and Storage System (SeaBASS). The corresponding SeaWiFS $nLw(\lambda)$ used to estimate $a_g(400)$ were matched to the *in situ* data by Sean W. Bailey (NASA Goddard Space Flight Center). The details of the match-up procedure can be found in Bailey and Werdell (2006). From this match-up analysis, we estimated an average absolute uncertainty of ±32% (quasi-normal distribution of error around a mean of 0%) for the retrieval of $a_g(400)$. Note that the match-up analysis was done for $a_g(400)$ because many $a_g(\lambda)$ spectra available through SeaBASS did not contain UV values.

2.2.4. $\phi_{CO}(\lambda)$

Numerous published carbon monoxide AQY spectra determined for inland (Gao & Zepp, 1998; Valentine & Zepp, 1993), coastal (Miller et al., 2002; Zhang et al., 2006; Ziolkowski & Miller, 2007) and open-ocean environments (Kettle, 1994; Zafiriou et al., 2003; Stubbins, Uher, Kitidis, et al., 2006; Ziolkowski & Miller, 2007) exhibit a surprisingly limited variability. The relatively small differences in the magnitude of AQY measured in the ocean allow us to use a single average AQY for the global surface ocean without introducing an excessive error in the calculated photoproduction rates. In this study, we use a generic quantum yield calculated as the mean of the aggregate quantum yields of Ziolkowski and Miller (2007), determined from multiple samples collected in the Gulf of Maine and the Middle Atlantic Bight (Eq. (7)), and that of Zafiriou et al. (2003) calculated from 15 samples collected along a 70°S–45°N transect in the Pacific ocean (Eqs. (8) and (9)). The difference between the generic AQY used here and the aggregate spectra of Zafiriou et al. (2003) and Ziolkowski and Miller (2007) is about ±25–30% (varying with wavelength) over the 290–490 nm range and ±18% on average in the UV region.

$$\phi_{CO}(\lambda) = e^{-(9.134 + 0.0425(\lambda - 290))} + e^{-(11.316 + 0.0142(\lambda - 290))} \tag{7}$$

$$\phi_{CO}(\lambda) = \left(5.78 \times 10^{-6}\right)e^{-0.05(\lambda - 360)} - 6.99 \times 10^{-7} \quad \lambda < 360\,\text{nm} \tag{8}$$

$$\phi_{CO}(\lambda) = \left(5.24 \times 10^{-6}\right)e^{-0.0229(\lambda - 360)} \quad \lambda > 360\,\text{nm}. \tag{9}$$

2.3. Calculation of depth-integrated rates

Photoproduction rates were integrated from the ocean's surface to the seasonal mixed layer depth (MLD) and over the entire range of the sunlit layer (SL) (layer of the ocean where solar radiation is present). Monthly climatologies of mixed layer depth for the global ocean constructed by the US Naval Research Laboratory (NRL) were used in this study. A detailed definition of the optimal mixed layer depth and details on the variability of the mixed layer depth in the NRL

climatologies can be found in Kara et al. (2000, 2003), respectively. Information can also be found on the US Naval Research Laboratory website (NRL, 2006). The optimal MLD is defined using a density-based criterion that accounts for variable temperature and salinity and was constructed from the 1° monthly-mean temperature and salinity climatologies of the World Ocean Atlas 1994 (Levitus & Boyer, 1994; Levitus et al., 1994). Fig. 4 displays the NRL MLD climatology for the month of April.

In order to account for all the photoproduction in the surface ocean, the bottom of the "sunlit layer" was defined as 1000 m or the depth of the seafloor whichever is less. The ETOPO5 5 minutes-gridded data set (National Geophysical Data Center) was used for bathymetry. Photoproduction of CO from sediments was ignored even though in shallow areas significant levels of photochemically active radiation can reach the bottom. Where the mixed layer extends to the bottom of the ocean the sunlit layer is equivalent to the mixed layer. In this manuscript, daily, depth-integrated rates for the mixed layer (ML) and for the sunlit layer (SL) are denoted $\tilde{\Psi}_{CO}^{Day}(ML)$ and $\tilde{\Psi}_{CO}^{Day}(SL)$, respectively.

3. Results

3.1. Spatio-temporal variability and depth distributions of CO photoproduction

Global maps of calculated CO photoproduction rates at the 0^- m and 20 m isodepths are displayed in Fig. 5. While climatologies were calculated for every month of the year, only the results for January, April and July are displayed in the figures. The spatial and seasonal patterns of CO photoproduction are complex but show clearly the relation between the attenuation of UV radiation in seawater (e.g. $K_d(320)$) and the vertical distribution of CO photoproduction in the surface ocean. As illustrated in Fig. 5, observed patterns are strikingly different depending on the isodepth considered. A comparison with the $K_d(320)$ patterns (Fig. 3) clearly demonstrates how photoproduction rates at the surface (0^- m) are higher in areas exhibiting high UV attenuation (and CDOM absorption since CDOM is the main scavenger of UV radiation in the ocean). In contrast, the photoproduction rates at 20 m are maximum in the clearest natural waters and in areas of high irradiances (e.g. subtropical gyres). Understandably, areas with high CDOM and diffuse attenuation coefficients restrict the number of photons available to promote photoproduction deeper within the water column. The control of the optical properties of seawater on the vertical distribution of CO photoproduction is better illustrated in Fig. 6 where photoproduction rate profiles from various water types are plotted together.

As can be inferred from the similarity between the global distributions of $E_{od}^{Day}(320, 0^-)$ (Fig. 3) and $\tilde{\Psi}_{CO}^{Day}(SL)$ (Fig. 7), the incident irradiance is the primary driver of the overall magnitude of the photoproduction within the entire sunlit layer of the ocean. Thus, while $\tilde{\Psi}_{CO}^{Day}(SL)$ is largely a function of the incident irradiance, the depth range over which photoproduction occurs is primarily controlled by diffuse attenuation coefficients in the UV domain, the variability of which is directly related to that of CDOM. The change in specific ratios between $K_d(\lambda)$ and $a_g(\lambda)$ at individual wavelengths other than $\lambda = 320$ nm also accounts for variability among depth-resolved rates by affecting the proportion of attenuated photons scavenged by CDOM (versus other seawater constituents).

Note that our interpretation of the spatio-temporal patterns of CO photoproduction is somewhat hampered by the use of a single, constant apparent quantum yield in our calculations. While the range of variability in published $\phi_{CO}(\lambda)$ for the ocean suggests that this assumption is acceptable for use in global estimates, a variable AQY would affect the magnitude of $\tilde{\Psi}_{CO}^{Day}(SL)$. The depth distribution of the rates, however, should remain unaffected as long as the water column is assumed homogeneous. Considering the results of Zhang et al. (2006), $\tilde{\Psi}_{CO}^{Day}(SL)$ patterns would no longer just mimic those of $E_{od}^{Day}(320, 0^-)$ but may also tend towards those of sea surface temperature. Nevertheless, the spatial variability in CO photoproduction rates resulting from changes in the incident irradiance is expected to dwarf the effects of variation in $\phi_{CO}(\lambda)$. Our interpretation is also limited by the assumption of a homogeneous water column with consequences for both the magnitude of $\tilde{\Psi}_{CO}^{Day}(SL)$ and the depth distribution of the rates (further discussed in Section 3.3).

3.2. Global budgets

Global and hemispheric budgets for CO photoproduction in the mixed layer and the sunlit layer can be estimated from the calculated $\tilde{\Psi}_{CO}^{Day}(ML)$ and $\tilde{\Psi}_{CO}^{Day}(SL)$ monthly climatologies, respectively. The total mass of carbon produced through marine photoproduction of CO over the course of one day and under monthly-averaged conditions, was calculated for both hemispheres and for the twelve months of the year. The estimates for the calculated global CO photoproduction rates are shown in Table 1 and have units of GgC day^{-1}. Details regarding the calculation of these numbers from the computed $\tilde{\Psi}_{CO}^{Day}(ML)$ and $\tilde{\Psi}_{CO}^{Day}(SL)$ are given in the caption of Table 1. Note that the area represented by each pixel varies as a function of latitude since our data are represented on a 500×1000 grid. The area corresponding to each pixel was computed as the product of the area of one pixel at the Equator (1600.62×10^6 m^2) and the cosine of the latitude (in radian). Regions where rates could not be calculated (gray areas in Figs. 5 to 8) were not included in the calculation of global rates. However, they generally correspond to relatively small areas at high latitudes (no more than 10% of the global ocean's surface area) either covered with ice or subject to minimal incident irradiance. We estimated that the underestimation associated with this limitation should be less than 1.5 TgC yr^{-1}. This estimate was obtained by assuming that the average photoproduction rate for these regions is equal to the average of the rates calculated for the pixels adjacent to these regions (average weighted for corresponding pixel area).

Yearly estimates for the two hemispheres (units of TgC yr^{-1}) were obtained by calculating the mean of the twelve month estimates and by multiplying by the average number of days in a year, 365.25, therefore assuming that variation between each consecutive month is linear. In the Northern hemisphere, minimum and maximum depth-integrated rates in the SL are reached in December and June, respectively, with December rates 2 times lower than June rates (31.9 and 64.3 GgC yr^{-1}, respectively). In the Southern hemisphere, however, minimum and maximum rates are reached in June and January, respectively, with June rates 3 times lower than January rates (31.5 and 89.4 GgC day^{-1}, respectively). On a yearly basis, the Northern hemisphere produces a total of 17.9 TgC yr^{-1} while the Southern hemisphere yields about 22.7 TgC yr^{-1} (27% more than the
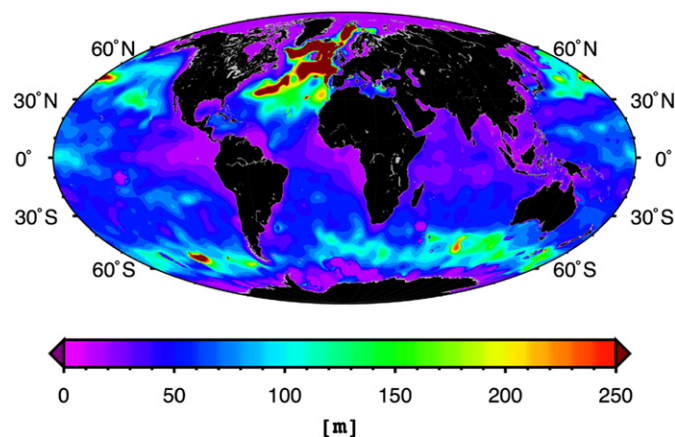

Fig. 4. Climatology of optimal mixed layer depth (Naval Research Laboratory MLD data) for April.
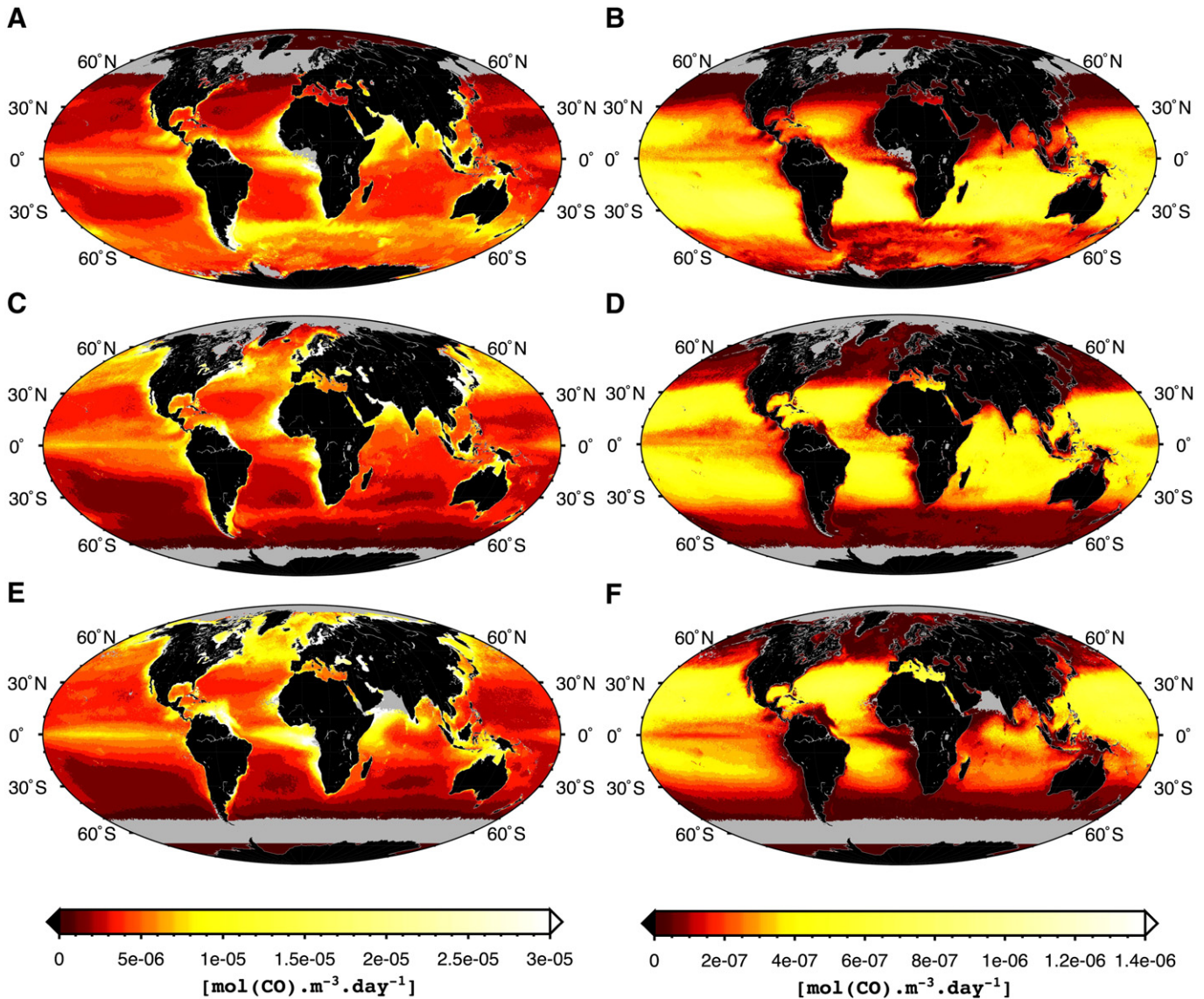
Fig. 5. Global maps of CO photoproduction rates calculated at the 0^- m and 20 m isodepths (left and right columns, respectively). Three different months are displayed: January (A, B), April (C,D) and July (E,F). Regions in gray represent areas where SeaWiFS ocean color is unavailable. Dark brown areas at the North Pole (January) and the South Pole (July) represent areas where photoproduction rates are null.

N.H.). The disparity between the two hemispheres is attributable not only to the larger surface area covered by oceans in the SH but also to the slightly closer proximity of the Earth to the Sun during the Southern hemisphere summer solstice.

Our global yearly estimate of 40.6 TgC yr^{-1} is thus in good agreement with a global "blue-water" photochemical source term range of 30–50 TgC yr^{-1} reported by Zafiriou et al. (2003) and with the recent open-ocean photoproduction average of 47 TgC yr^{-1} calculated by Stubbins, Uher, Law, et al. (2006). Assuming that coastal waters (where water depth is <200 m) represent 9% of the global ocean's surface area, we estimate a total "coastal-water" CO photoproduction rate of about 3.0 TgC yr^{-1}. Our estimate is significantly lower than that of Zafiriou et al. (2003) and accounts for about 7.5% of the global rate. The "coastal-water" rate also exhibits a significant seasonal variability (with minimum in wintertime) resulting from the much larger area covered by coastal waters in the Northern hemisphere. The contribution of coastal waters to the total CO photoproduction budget is therefore very seasonal.

Photoproduction of CO in sea ice and in ocean bottom sediments was not included in the budgets. To the extent of our knowledge, CO photoproduction from marine sediments has not been documented before. However, its contribution to global CO photoproduction is likely not significant since very little of the ocean floor is exposed to significant levels of UV radiation. In first-year ice, however, photoproduction rates of CO fifteen times higher than in adjacent open waters have been observed. As a result, the Arctic alone could potentially contribute 0.17 TgC yr^{-1} to the atmosphere (Xie & Gosselin, 2005).

The fate of photoproduced CO heavily depends on its removal from the surface ocean via microbial consumption and air–sea gas exchange. Venting to the atmosphere requires CO to be in proximity to the sea–air interface while microbial consumption occurs at all depths. Since consumption results in turnover times ranging from <1 h in warm productive areas to >90 h in cold waters (Xie et al., 2005), it is reasonable to assume that almost all of the CO produced below the mixed layer is bio-oxidized and unavailable for transfer to the atmosphere. An estimate of CO unavailable to atmospheric transfer can be obtained by assessing how much of the total water column photoproduction takes place below the mixed layer ($\tilde{\Psi}_{CO}^{Day}(SL)$ and $\tilde{\Psi}_{CO}^{Day}(ML)$).

Global maps of $\tilde{\Psi}_{CO}^{Day}(ML)$ for January, April and July are displayed in Fig. 8 along with the corresponding global maps of the $\tilde{\Psi}_{CO}^{Day}(ML)/\tilde{\Psi}_{CO}^{Day}(SL)$ ratio shown as a percentage. Our global and hemispheric
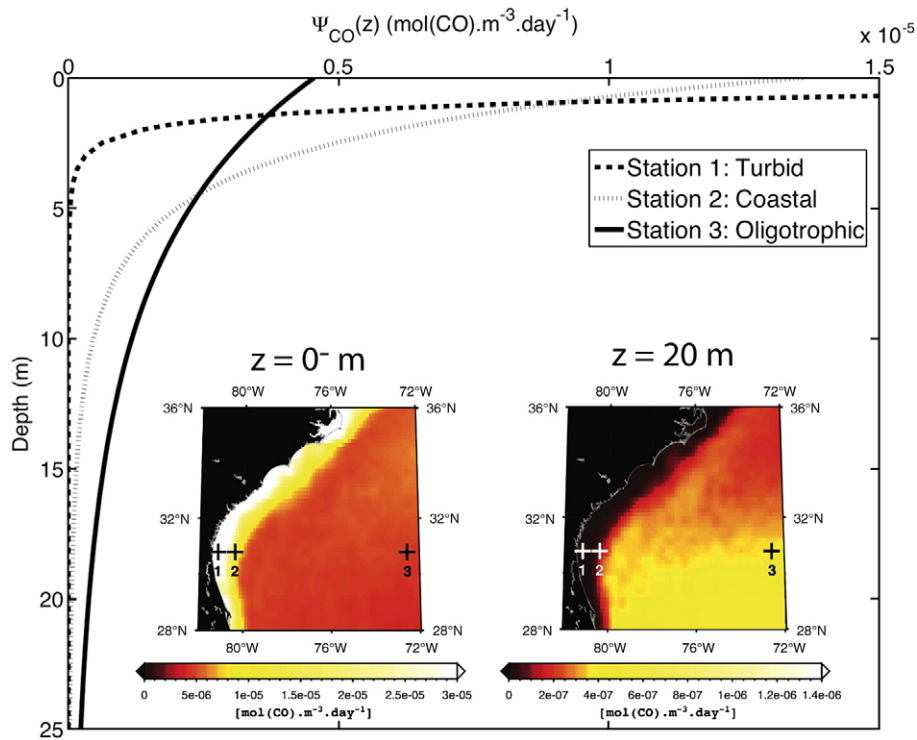
Fig. 6. Dependence of CO photoproduction rate profiles on the diffuse attenuation coefficients. Three stations are used as examples to illustrate this concept. The stations are contrasting in terms of optical properties but receive very similar levels of irradiance (constant latitude). Station 1: $K_d(320)=2.55$ m^{-1}, Station 2: $K_d(320)=0.51$ m^{-1}, Station 3: $K_d(320)=0.18$ m^{-1}.

estimates (Table 1) show that, on average, 96% (range from 94 to 99%) of all the photoproduction occurs within the mixed layer. However, as illustrated by the $\tilde{\Psi}_{CO}^{Day}(ML)/\tilde{\Psi}_{CO}^{Day}(SL)$ maps, the percentage of photoproduction occurring below the mixed layer (% of $\tilde{\Psi}_{CO}^{Day}(SL)$ in ML) can reach 20–40% over large areas of the ocean. Such areas typically include the subtropical gyres during the summer months where the combination of a shallow mixed layer and low attenuation by seawater constituents allows significant levels of UV radiation to reach well below the mixed layer depth. This observation is in good agreement with the recent finding by Zafiriou et al. (2008) that 30% of the CO burden is located below the mixed layer in the Sargasso Sea during summertime. The Mediterranean Sea, the Gulf of Mexico and the Sea of Japan also exhibit such patterns in summer.

3.3. Uncertainties in estimated rates

The validation of our photoproduction model and of its implementation on a global scale remains a difficult task. An end-to-end validation of a single CO photoproduction profile would require a day-long deployment of mooring under clear-sky conditions and coincident with overpass of ocean color satellites for proper match-up. While efforts towards the acquisition of a representative validation dataset should be pursued, it is possible at this stage to estimate a theoretical error in the calculated rates by conducting a meaningful sensitivity analysis to evaluate the dependence of critical model outputs such as $\Psi_{CO}^{Day}(0^-)$, $\Psi_{CO}^{Day}(20\,m)$, $\tilde{\Psi}_{CO}^{Day}(ML)$ and $\tilde{\Psi}_{CO}^{Day}(SL)$ to errors in the model inputs: $E_{od}^{Day}(\lambda, 0^-)$, $K_d(\lambda)$, $a_g(\lambda)$ and $\phi_{CO}(\lambda)$. Note that although $a_g(320)$ is derived from $K_d(320)$ using a single ratio, $a_g(\lambda)$ vary independently from $K_d(\lambda)$ at wavelengths other than $\lambda = 320$ nm. We therefore treat $a_g(\lambda)$ as an independent input.

The method used for the sensitivity analysis is explained in detail in Appendix B. Realistic errors associated with the inputs are most likely a combination of spectrally correlated and spectrally uncorrelated noise. In other words, the percentage error is expected to vary significantly as a function of wavelength. The results of the sensitivity analysis in

Table 2 demonstrates the effects of spectrally correlated (skew in the whole spectrum) versus spectrally uncorrelated (the error is different at every wavelength) noise on the outputs of the model. A much larger error is associated with the outputs if noise added to the inputs is 100% spectrally correlated. Adding noise that is uncorrelated tends to considerably reduce the propagation of error in the outputs of the model. This is observed because outputs are calculated as the product of inputs and are integrated over the 290 and 490 nm spectral range. Noise that is different at every wavelength therefore tends to cancel out in such a calculation. In Section 2.2 we also estimated the uncertainties in the inputs to be 30% for $E_{od}^{Day}(\lambda, 0^-)$, 30% for $K_d(\lambda)$, 32% for $a_g(400)$ and 25–30% for $\phi_{CO}(\lambda)$. The case where an average 30% error in every input is 50% correlated and 50% uncorrelated therefore serves as our most representative error estimate. For such a case, the error in the outputs ranges ± 23–49% depending on the product considered (Table 2). $\Psi_{CO}^{Day}(20\,m)$ is most sensitive because of its greater dependence on errors in the diffuse attenuation coefficients.

We also proceeded to a sensitivity analysis by adding noise in only one of the input at a time. When a 30% uncertainty (with $C = 0.5$, $U = 0.5$) is added to either $E_{od}^{Day}(\lambda, 0^-)$, $a_g(\lambda)$ and $\phi_{CO}(\lambda)$, we estimate that all four outputs are retrieved within ± 13–16%. However, because $K_d(\lambda)$ controls the vertical distribution of photoproduction, a 30% uncertainty in this input leads to a variable error depending the output considered: $\Psi_{CO}^{Day}(0^-)$ is unaffected, $\tilde{\Psi}_{CO}^{Day}(ML)$ and $\tilde{\Psi}_{CO}^{Day}(SL)$ are estimated within ± 13–14% and $\Psi_{CO}^{Day}(20\,m)$ within $\pm 30\%$.

In addition to the uncertainty we just described, the use of a practical photochemical model (Eq. (5)) and its implementation using a relatively coarse spectral and vertical resolution (see Section 2.2) introduces some additional error in our estimates relative to the implementation of the general model (Eq. (4)) using a very fine resolution. However, based on our error estimates given in Section 2, the overall uncertainty should rarely exceed 10%.

Finally, another source of uncertainty in our estimated rates originates from the assumption that $K_d(\lambda)$, $a_g(\lambda)$ and $\phi_{CO}(\lambda)$ are assumed to remain constant with depth. In Section 2.2 we justify this
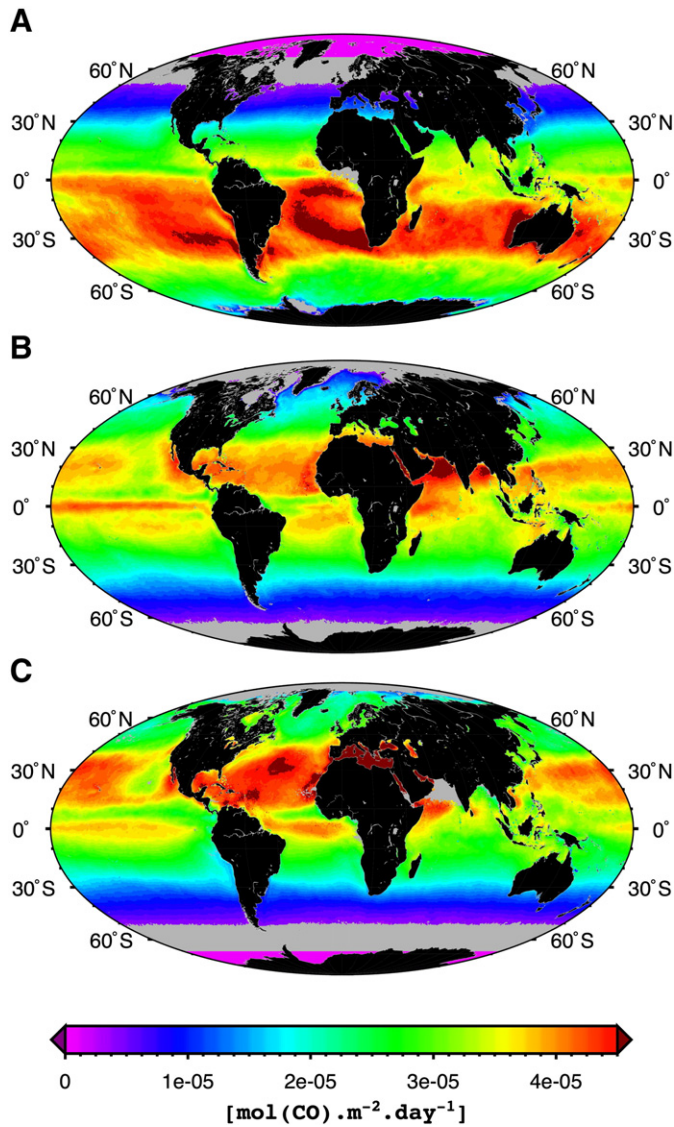
A

B

C

Fig. 7. Global maps of depth-integrated CO photoproduction rates calculated for the sunlit layer. Three different months are displayed: January (A), April (B) and July (C). Regions in gray represent areas where SeaWiFS ocean color is unavailable. Purple areas at the North Pole (January) and the South Pole (July) represent areas where photoproduction rates are null.

assumption by stating that variables retrieved using remote sensing (e.g. $K_d(\lambda)$, $a_g(\lambda)$) are average values representative of a layer extending from the surface to the first optical depth. Because most solar radiation is attenuated within this layer (by definition), it is also where most of the photoproduction occurs. As a result, the variables retrieved from remote sensing are averages representative of the layer over which most of the photoproduction occurs. Therefore, in as much as it is acceptable to assume this layer to be homogeneous in terms of these properties (e.g. when calculating a climatology), the error associated with this assumption should be minimal as it only affects the magnitude of rates below the first optical depth. In order to assess the impact of this assumption, we compared the results of our model to a version of the model that includes variations in $a_g(\lambda)$ and $K_d(\lambda)$ below the first optical depth. Tests were made using both linear and quadratic three-fold increases and decreases in $a_g(\lambda)$ between the first optical depth and the 100 m depth (maximum observed vertical variations in $a_g(325)$ or $a_g(320)$ observed by Nelson et al. (2007) and Yamashita and Tanoue (2009) in the North Atlantic and North Pacific, respectively). The variability in $K_d(320)$ was constrained by that of $a_g(320)$, although the ratio $a_g(\lambda)/K_d(\lambda)$ was allowed to vary more freely at other wavelengths. A vertical linear increase or decrease of 30% in $\phi_{CO(\lambda)}$ was assumed in these calculations. Using a representative range of inputs to the model, our results indicate that this assumption never introduces errors higher than $\pm 3\%$ for $\tilde{\Psi}_{CO}^{Day}(SL)$ and $\tilde{\Psi}_{CO}^{Day}(ML)$ and $\pm 15\%$ for $\Psi_{CO}^{Day}(20\,m)$.

4. Discussion

4.1. Assessing the role of CO in global biogeochemical cycles

CO photoproduction is generally envisioned as a direct pathway for the remineralization of the oceanic DOC pool (Kieber et al., 1989; Mopper & Kieber, 2001; Mopper et al., 1991). Our global CO photoproduction estimate of 40.6 TgC yr^{-1} would thus correspond to a maximum remineralization of about 0.2% of the total DOC produced annually in the global ocean, if a global primary production rate of 50 PgC yr^{-1} with a 50% rerouting through the DOC loop is assumed. In reality, the fate of photochemically derived CO depends heavily on its removal mechanisms which ultimately control its role in global biogeochemical cycles. The two major sinks of CO in the ocean are venting to the atmosphere and consumption by the microbial community (Zafiriou et al., 2003). An important aspect that is often overlooked in global budgets of CO in the ocean is the dependence of the relative magnitude of the sink processes on the vertical distribution of CO. Indeed, CO produced closer to the surface has

Table 1
Depth-integrated photoproduction rates in the mixed layer (ML) and the sunlit layer (SL) for the two hemispheres and the global ocean. Note that for each month the average rate is given in units of GgC day^{-1} while the average rate for the year is given in units of TgC yr^{-1}. For both hemispheres and for every month, Ψ_{CO}^{Day} (ML) and Ψ_{CO}^{Day} (SL) were multiplied by the area (in m^2) corresponding to their pixel (to account for variation with latitude) and then summed. A molar mass of carbon equal to 12.01 g mol^{-1} was used to convert rates from units of mol(CO) day^{-1} to units of gC day^{-1}.

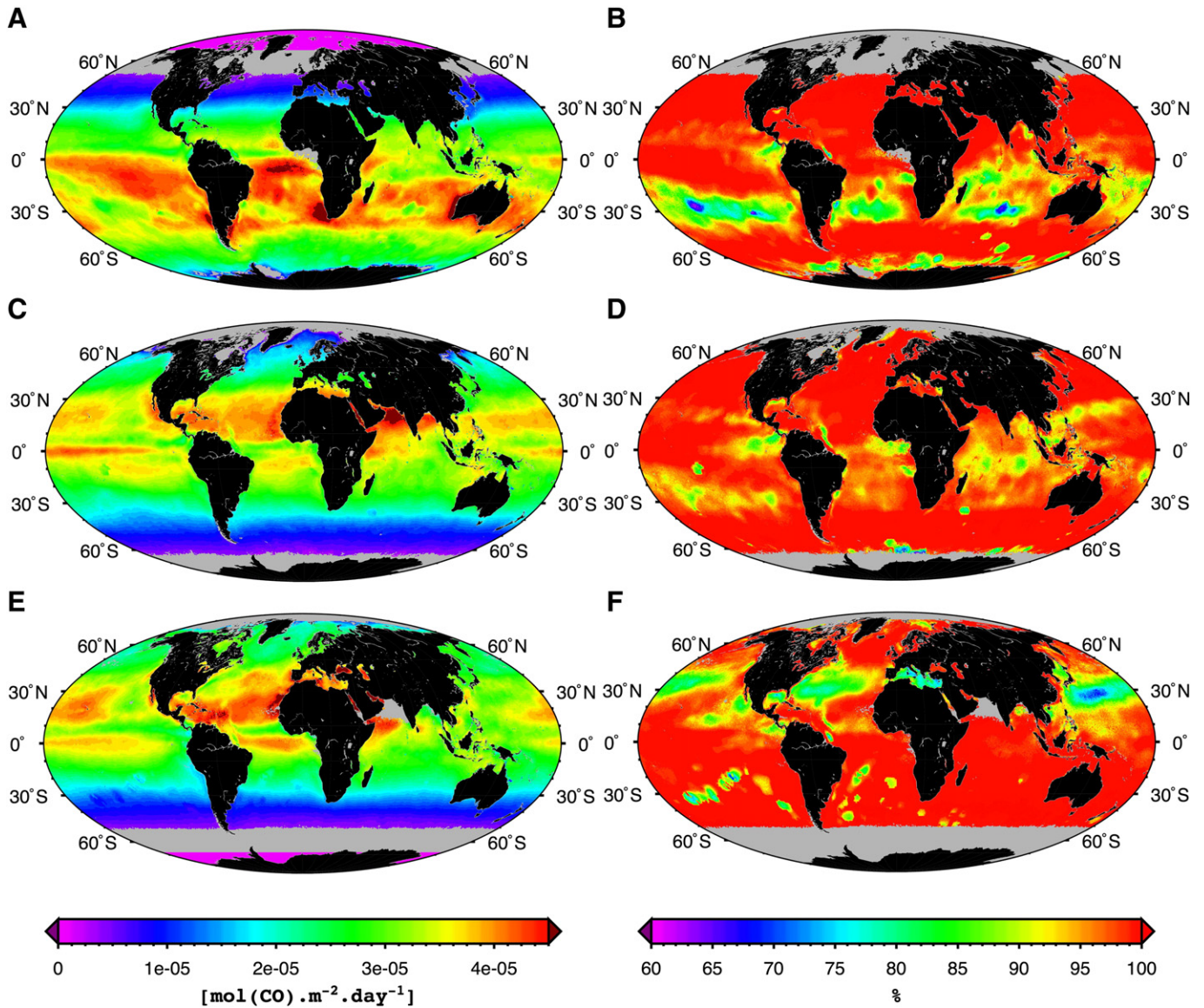|	Jan	Feb	Mar	Apr	May	Jun	Jul	Aug	Sep	Oct	Nov	Dec	Year
	GgC day^{-1}												TgC yr^{-1}
Northern hemisphere (N.H.)													
ML	34.2	41.7	49.2	53.9	58.0	60.3	55.7	54.4	49.9	43.0	34.9	31.3	17.3
SL	34.7	42.2	50.0	55.1	60.0	64.3	59.4	57.9	52.6	44.7	36.1	31.9	17.9
Southern hemisphere (S.H.)													
ML	84.6	76.1	64.3	50.2	40.1	31.0	36.8	45.6	59.1	71.2	79.8	84.8	22.0
SL	89.4	80.0	67.3	51.8	40.9	31.5	37.2	46.1	59.5	72.0	81.8	88.3	22.7
Global (N.H. + S.H.)													
ML	118.8	117.8	113.5	104.1	98.1	91.3	92.5	100.0	109.0	114.2	114.7	116.1	39.3
SL	124.1	122.2	117.3	106.9	100.9	95.8	96.6	104.0	112.1	116.7	117.9	120.2	40.6

Fig. 8. Global maps of mixed layer photoproduction rates and percentage of total depth-integrated photoproduction rate occurring in the mixed layer (left and right columns, respectively). Three different months are displayed: January (A,B), April (C,D) and July (E,F). Regions in gray represent areas where SeaWiFS ocean color is unavailable. Purple areas at the North Pole (January) and the South Pole (July) represent areas where photoproduction rates are null.

Table 2

Sensitivity of the model products having 10, 30 or 50% of correlated ($C=1$), uncorrelated ($U=1$) and mixed ($C=0.5$, $U=0.5$) noise added to the inputs. Note that the median of the error distribution (in terms of percentage difference with the unaltered estimates) is used rather than the mean.

	Ψ_{CO}^{Day} $(0^-\,m)$	Ψ_{CO}^{Day} (20 m)	$\tilde{\Psi}_{CO}^{Day}$ (ML)	$\tilde{\Psi}_{CO}^{Day}$ (SL)
$\Upsilon=0.1$ ($=10\%$ error added to inputs)				
$U=1, C=0$	±4%	±7%	±4%	±4%
$U=0, C=1$	±15%	±24%	±17%	±17%
$U=0.5, C=0.5$	±8%	±13%	±9%	±9%
$\Upsilon=0.3$ ($=30\%$ error added to inputs)				
$U=1, C=0$	±13%	±48%	±18%	±26%
$U=0, C=1$	±46%	±67%	±51%	±52%
$U=0.5, C=0.5$	±23%	±39%	±27%	±27%
$\Upsilon=0.5$ ($=50\%$ error added to inputs)				
$U=1, C=0$	±23%	±70%	±31%	±45%
$U=0, C=1$	±78%	±94%	±86%	±87%
$U=0.5, C=0.5$	±39%	±65%	±47%	±54%

greater potential of escaping to the atmosphere while CO produced at depth (especially below the mixed layer depth) is more likely to be consumed by the microbial community.

Field measurements of CO supersaturation in the surface ocean have motivated scientists to estimate fluxes of CO from the ocean to the atmosphere. The dynamics of sources and sinks are such that CO concentrations in the surface ocean usually follow a diurnal pattern with maximum near-surface ocean concentrations greatly exceeding saturation during daylight (Ohta, 1997). Although vertical mixing tends to redistribute CO in the water column, vertical profiles of CO in sunlit waters are primarily dictated by the photoproduction source rather than the sinks. Measured *in situ* profiles of CO concentrations are often observed to decrease exponentially with depth (Kettle, 2005; Ohta, 1997; Zafiriou et al., 2008).

While CO is not considered a greenhouse gas, it does represent an important control on atmospheric hydroxyl radical (OH•) concentration, where about 90% of atmospheric CO reacts with OH• to form carbon dioxide. This process and the reaction of OH• with methane are

the major pathways by which OH• is removed from the atmosphere. As a result, CO indirectly affects the atmospheric burden of methane by competing for tropospheric OH•. It has thus been suggested that an emission of 100 Tg of CO would equate to a release of 5 Tg of methane (IPCC, 2001). For years, there have been discrepancies regarding the global oceanic CO source strength to the atmosphere with estimates ranging from 13 TgC yr^{-1} up to 1200 TgC yr^{-1} (Erickson, 1989; Bates et al., 1995; Zuo & Jones, 1995; Springer-Young et al., 1996). Although the estimate of 1200 TgC yr^{-1} by Springer-Young et al. (1996) was based on the unlikely assumption that practically all photochemically produced CO escaped to the atmosphere, upper range estimates mainly stem from uncertainties associated with the magnitude of the photoproduction term. In the last few years, however, several independent studies (including the present one) have converged on a refined range of 30–84 TgC yr^{-1} (Fichot, 2004; Stubbins, Uher, Law, et al., 2006; Zafiriou et al., 2003) for global ocean CO photoproduction. Considering that only a fraction of this CO escapes to the atmosphere, these newer estimates tend toward a reduced oceanic source term to the atmosphere (3.7 ± 2.6 TgC yr^{-1} as estimated by Stubbins, Uher, Kitidis, et al., 2006).

While CO vented to the atmosphere directly affects the atmospheric burden of methane (and CO_2 via its reaction with OH•), the role of biologically oxidized CO in biogeochemical cycling is more complex and less well understood and quantified. Newly discovered metabolic strategies in marine bacteria suggest that CO is used primarily as a source of energy rather than a source of carbon by the microbial community (Tolli et al., 2006). This bio-oxidation of CO would thus represent a direct source a CO_2 in the ocean and maintain the remineralization pathway initiated by photochemistry. From a biological point of view, the ability to oxidize CO would enhance bacterial production by providing an alternate energy source to heterotrophic bacteria (a process called lithoheterotrophy) (Moran & Miller, 2007). However, new data on bacterial CO consumption presents a paradox for microbial ecology. There is evidence that the gene responsible for CO oxidation may be expressed constitutively by members of the Roseobacter clade which is ubiquitous in the marine environment (Johnson, 2007). Moran and Miller (2007), however, have recently compared photochemical production of CO in coastal waters to the potential energetic benefit for coastal bacteria and estimate that CO can supply at best 1% of bacterial energy demand.

Despite the open question of why bacteria invest energy to express genes for CO oxidation when the potential benefit appears to be small, measured microbial consumption rates lead to the conclusion that bio-oxidation is the dominant sink for CO under normal oceanic mixing conditions (Zafiriou et al., 2003). However, the relative magnitude of both gas exchange and bio-oxidation exhibits strong spatial and temporal variabilities. Fluxes of CO to the atmosphere from the ocean depend on sea surface temperature, salinity, and especially on windspeed and the gradient of CO concentration between the sea surface and the overlying atmosphere. Daily sea-to-air fluxes estimated in the Atlantic Ocean by Stubbins, Uher, Kitidis, et al. (2006) thus varied from 0.4 to 12.1 µmol(CO) m^{-2} day^{-1} for the Atlantic ocean in April/May alone and scaled strongly with windspeed. Microbial CO consumption rate constants measured in various marine environments have been shown to vary from at least 0.011 to 2.44 h^{-1} (corresponding to turnover rates of 95 and 0.4 h, respectively) (Xie et al., 2005). Factors affecting the CO consumption rate constant include temperature, pH, bacterial population density, species composition and availability of organic substrates and nutrients.

Evaluating the role of CO photoproduction in global biogeochemical cycles requires better constraints on the depth distribution of the source term of carbon monoxide. The depth of the mixed layer relative to that of the entire sunlit layer is therefore of particular importance. Under conditions where solar radiation is strongly attenuated most photoproduction is restricted to the surface layer while photoproduction can remain significant below the mixed layer in clearer, oligotrophic waters.

Proper quantification of the sinks however requires the development and validation of models of the daily cycle of CO incorporating vertical mixing, sea–air gas exchange and bacterial consumption to fully comprehend and quantify the daily cycle production/removal of CO. Although such complex models have been developed and tested in localized areas (Kettle, 2005; Zafiriou et al., 2008), assessing the role of CO in global biogeochemical cycles over larger spatio-temporal scales is achievable by combining remote sensing and robust models such as the one presented in this paper.

4.2. Quantifying marine photochemical fluxes using remote sensing

The data and discussion presented for CO photochemistry in this paper result from a progressive convergence of research in ocean optics and marine photochemistry. It is clear that for the methods used here to produce useful insight on the spatial and temporal importance of photochemistry in the ocean, both spectral radiation distributions and photochemical reactions must be addressed accurately and quantitatively.

Application of the Sea*UV*/Sea*UV$_C$* algorithms (Fichot et al., 2008) can provide a good approximation of the depth-resolved UV radiation field in diverse types of oceanic waters. It represents a simple approach that can be relatively easy to implement with remotely sensed ocean color data. Even though the quality of its output can only be as good as the remotely sensed data to which it is applied, it does represent a significant advance in accurately quantifying the full effect of solar radiation ($\lambda = 290–490$ nm) on marine biogeochemical cycles. As algorithms and hardware are improved for satellite remote sensing, and as more *in situ* optical data for UV penetration into the sea is obtained, these estimates of the spectral radiation field that drives both photochemical and photobiological reactions will increase in accuracy. While we have shown this method to be very promising for quantifying marine photochemistry (CO in particular), it is hampered significantly for general application by the current lack of knowledge about the natural variability in the quantum yield spectra for many photochemical products.

Our current inability to properly constrain the natural variability of $\phi_{CO}(\lambda)$ in the ocean represents the major limitation in the accurate quantification of $\Psi_{CO}^{Day}(z)$. New data that show a strong relation between CO photoproduction and DOM aromaticity (Stubbins et al., 2008) contribute to a mechanistic rationale for the low degree of variability observed for CO AQY from dissimilar water types. If CO photoproduction and the absorption of radiation by CDOM both depend on aromaticity, then measured AQY (the ratio of CO production to photon absorbance by CDOM) will remain fairly constant even as organic mixtures vary. A first step towards a better understanding of the factors influencing this variability was accomplished by Zhang et al. (2006) by examining the effects of temperature and CDOM quality on $\phi_{CO}(\lambda)$ along a 0–33 salinity gradient (St-Lawrence estuary, Canada). Zhang et al. (2006) concluded that while photobleaching and CDOM source have limited effects on AQY, a 20 °C temperature change could potentially alter the solar insolation-weighted mean AQY by up to 30–40% in marine waters. Because this study is restricted to the St-Lawrence estuary, however, the application of a correction factor for the possible temperature dependence of our $\phi_{CO}(\lambda)$ seems inadequate. Since our calculations are made for the global ocean, our generic AQY (generated from those of Zafiriou et al., 2003 and Ziolkowski & Miller, 2007) seems most appropriate.

All of this gives us a better understanding by which to constrain AQY variability in the prediction of CO photochemistry in the world oceans. Similar constraints for almost every other marine photochemical process are lacking due to limited mechanistic knowledge and few published AQY spectra obtained in diverse marine environments. AQY spectra or the photochemical oxidation of DOC to DIC have been published for a limited number of marine and fresh waters (Bélanger et al., 2006; Johannessen & Miller, 2001; Vähätalo et al., 2000). Current indications are that AQY spectra for this process vary

significantly more than those for CO. This may result from varying organic source material or from a fundamental disconnect between the moiety responsible for DIC production and radiation absorbance by CDOM (unlike CO) as suggested by Johannessen and Miller (2001). Variations of AQY spectra for the photochemical destruction of DMS have been shown to vary strongly with both CDOM and nitrate concentrations (Bouillon & Miller, 2004; Bouillon & Miller, 2005; Deal et al., 2005). Both of these important photochemical processes present difficult challenges for using remote sensing to estimate their *in situ* rates with current methods. The Sea*UV*/Sea*UV$_C$* model predicts UV attenuation and CDOM absorption, both of which are used with AQY spectra to estimate photochemical rates in the approach presented in this paper. Those processes that do not scale directly with CDOM must include other data to account for variability in diverse ocean systems. For example, until nitrate concentrations can be estimated accurately from remote sensing or defined optical domains can be related to the presence of DIC/CO_2 photochemical precursors, using this approach to quantify DMS photolysis or DIC photoproduction on large scales will face serious limitations.

Another photoproduct for which *in situ* rate estimates calculated from remote sensing data should be feasible using the approach we present here is hydrogen peroxide (H_2O_2). Hydrogen peroxide has received a great deal of study and initial reports seemed to indicate a large variability of AQY spectra for H_2O_2 photoproduction in various oceanic locations. Miller (2000), however, showed that variations of AQY for this secondary photoproduct resulted from changes in water temperature. Additionally, the temperature dependence is accurately described using an Arrhenius relationship. Consequently, by blending remotely sensed sea surface temperature data with our Sea*UV*/Sea*UV$_C$* approach, the appropriate AQY spectrum for a given location can be accurately retrieved. Creative combinations of multiple remote sensing products for examining photochemical processes in the ocean will certainly lead to new insight. But as is the case for H_2O_2 and CO, a better understanding of photochemical mechanisms and their relationships to the optical and chemical properties for the diverse oceanic waters of interest is required to continue progress with accurate evaluation of the role of photochemistry in biogeochemical cycles.

5. Conclusion

We calculated a monthly climatology of depth-resolved photo-production rates of carbon monoxide for the global ocean using the high temporal and spatial coverage offered by the SeaWiFS and TOMS satellites. The results of the model provide us with a global estimate of 40.6 TgC yr^{-1}, more than 95% of which occurs within the mixed layer. The climatologies also provide us with a synoptic view of the spatial and temporal variabilities of CO photoproduction rates in the global ocean and clearly demonstrate how depth-integrated rates are mostly a function of the incident irradiance while the depth distribution of the rates is mainly controlled by the optical properties of the water mass considered. The capability of the model to estimate depth-resolved rates represents an important advantage in the attempt to constrain the sink mechanisms which ultimately determine the fate of CO and its role in global biogeochemical cycles. Slight variations to the model may be used to model other photochemical processes and also other effects of UV/visible solar radiation on biology and other sensitive systems. At this stage, the applicability of this model in the field of marine photochemistry is mostly limited by our lack of knowledge about the processes regulating the variability in the apparent quantum yields of the processes of interest.

Appendix A. Calculation of daily-integrated, cloud-corrected, just-below-surface downwelling scalar irradiance

The outputs of the System for the Transmission of Atmospheric Radiation (STAR) are clear-sky, global ($=$direct$+$diffuse fractions) downwelling irradiance spectra reaching the air–sea interface, $E_d^{cs}(\lambda, 0^+)$, at every nanometer in the $\lambda = 280$–700 nm spectral range. In order to derive irradiances usable for marine photochemical calculations, $E_d^{cs}(\lambda, 0^+)$ needs to be corrected for several factors: 1) the presence of clouds in the atmosphere; 2) the transmission of radiation through the air–sea interface; 3) the conversion to scalar irradiance. In the following, we explain the methods we used to convert $E_d^{cs}(\lambda, 0^+)$ into daily-integrated, cloud-corrected, just-below-surface downwelling scalar irradiance $E_{od}^{Day}(\lambda, 0^-)$.

The presence of clouds in the atmosphere generally contributes to the attenuation of downwelling irradiance through absorption and backscattering. Here, the effects of clouds were accounted for by using monthly-averaged UV reflectivities collected by TOMS from 1996 until December 2003 (Herman & Celarier, 1997) and from which monthly climatologies of UV reflectivities were computed. A correction factor, Γ, used to convert clear-sky to cloud-corrected irradiances was then derived from UV reflectivity monthly climatologies following the method of Eck and Dye (1991) and Eck et al. (1995):

$$\Gamma = 1 - \frac{(R - 0.05)}{0.9}, \tag{10}$$

where R is the TOMS measured UV reflectivity at $\lambda = 360$ and 380 nm. Γ is assumed to be constant over the course of a month and to be independent of wavelength. Note that this assumption of wavelength independence is justified by the fact that Eck and Dye (1991) and Eck et al. (1995) use the same approach to estimate a correction factor for Photosynthetic Active Radiation (PAR) and UV irradiance, respectively.

The product of $E_d^{cs}(\lambda, 0^+, t)$ and Γ provides an estimate of above-surface downwelling irradiances corrected for the attenuation by clouds. However, although a monthly-average correction factor can be used to provide reasonable estimates of the attenuation of monthly-average irradiances by clouds, another factor to consider is the change in the relative fractions of diffuse and direct irradiance reaching the air–sea interface. Changes in the fraction of diffuse incident irradiance reaching the air–sea interface have implications in the computation of transmittance through the air–sea interface and in the conversion to scalar irradiance. Changes in cloud cover and solar zenith angle affect the relative fractions of diffuse and direct irradiance in a complex fashion. For example, even under constant cloud cover, variations in the solar zenith angle will cause variations in the fractions over the course of a day. In the following paragraphs, we attempt to include the combined effect of changes in solar zenith angle and cloud cover in our calculation of $E_{od}^{Day}(\lambda, 0^-)$.

The solar zenith angle above the sea surface, θ_o, and the fraction of diffuse contributions to global downwelling irradiance just above the sea surface and under clear-sky conditions, $f_{diff}(\lambda, 0^+)$, are also outputs of the STAR model (for every hour of the day). We used the method of Grant and Gao (2003) (Eq. (6) of their manuscript) to correct for the change in $f_{diff}(\lambda, 0^+)$ attributable to the presence of clouds, assuming a constant cloud cover over 24 h. We used their UVB parameters to correct the diffuse fraction in the $\lambda = 290$–320 nm

range and their UVA parameters for the $\lambda = 320$–490 nm range. We assumed a linear relationship between TOMS UV reflectivities and the cloud cover fraction used by the method of Grant and Gao (2003).

The transmittance at the air–sea interface, $T(\lambda, t)$ (unitless), needs to be computed for every hour of the day in order to match the time resolution of the modeled $E_d^{cs}(\lambda, 0^+)$ and be properly accounted for. Under the assumption of a flat ocean, the transmittance at the air–sea interface and at time t, $T(\lambda, t)$, was estimated as follows:

$$T(\lambda, t) = f_{diff}\left(\lambda, 0^+, t\right) T_{diff} + \left(1 - f_{diff}\left(\lambda, 0^+, t\right)\right) T_{dir}(t) \quad (11)$$

where the transmittance of the diffuse fraction, T_{diff}, was assumed equal to 0.934, and the transmittance of the direct component, T_{dir}, is estimated using Fresnel's law of unpolarized light and is dependent on θ_o and the refractive indices of air and seawater. The effect of wind-roughened surface on the transmittance of direct radiation is generally very small except when $\theta_o > 70°$ (Austin, 1974). However, since global irradiances are usually low whenever $\theta_o > 70°$, the error associated with the assumption of a flat ocean should be minimal when dealing with daily-integrated irradiances. Note that whenever θ_o is high for most of the day (e.g. at high latitudes), the impact of this assumption should be tempered by the small fraction of direct incident irradiance. Note that the $f_{diff}(\lambda, 0^+, t)$ used in Eq. (10) was corrected for the effects of clouds.

Finally, the conversion to scalar irradiance requires to estimate the underwater average cosine for downwelling irradiance, $\bar{\mu}_d(\lambda, t)$ (unitless), at a temporal resolution that also matches that of $E_d^{cs}(\lambda, 0^+)$ (every hour). As in Huot et al. (2000) and Miller et al. (2002), we used a modified version of the empirical relationship of Prieur and Sathyendranath (1981) between $1/\bar{\mu}_d(\lambda, t)$, $f_{diff}(\lambda, 0^+)$ and the refracted solar zenith angle, $\theta_r(t)$, to derive $\bar{\mu}_d(\lambda, t)$ as follows:

$$\frac{1}{\bar{\mu}_d(\lambda, t)} = \frac{1 - f_{diff}(\lambda, t)}{\cos(\theta_r(t))} + \frac{f_{diff}(\lambda, t)}{0.859} \quad (12)$$

where $f_{diff}(\lambda, 0^+, t)$ is also corrected for clouds.

Thus, the product of $E_d^{cs}(\lambda, 0^+, t)$, Γ, $T(\lambda, t)$ and $1/\bar{\mu}_d(\lambda, t)$ yields hourly $E_{od}(\lambda, 0^-, t)$. Modeled $E_{od}(\lambda, 0^-, t)$ were then integrated over time (24 h) in order to obtain daily-integrated $E_{od}^{Day}(\lambda, 0^-)$. Note that prior to integration, the variables were interpolated to a 1 s time resolution (cubic interpolation) for a more accurate integration. The estimation of daily-integrated below-surface scalar downwelling irradiance from the modeled irradiance is summarized in Eq. (13):

$$E_{od}^{Day}(\lambda, 0^-) = \int_{Day} \frac{\Gamma E_d^{cs}(\lambda, 0^+, t) T(\lambda, t)}{\bar{\mu}_d(\lambda, t)} dt. \quad (13)$$

Appendix B. Sensitivity analysis

In order to carry out a relevant sensitivity analysis, we computed monthly climatologies of depth-resolved CO photoproduction rates using altered inputs (original inputs to which noise has been added) and compared them to the original climatologies presented in this study. The altered inputs were estimated by adding noise to the original variables using Eq. (14):

$$\hat{V}(\lambda) = V(\lambda) + V(\lambda)\varepsilon(\lambda)\Upsilon, \quad (14)$$

where $\hat{V}(\lambda)$ and $V(\lambda)$ represent the altered and original variables, respectively, Υ is the set percentage error (relative mean absolute deviation in terms of percentage) and $\varepsilon(\lambda)$ is given in Eq. (15):

$$\varepsilon(\lambda) = U\varepsilon_u(\lambda) + C\varepsilon_c, \quad (15)$$

where $\varepsilon_u(\lambda)$ and ε_c are normal distributions of mean $\mu = 0$ and standard deviation $\sigma = 1/\sqrt{(2/\pi)}$ (since Υ is expressed in terms of mean

absolute deviation rather than standard deviation), U and C are the fractions of correlated and uncorrelated noise ($U + C = 1$). Note that $\varepsilon_u(\lambda)$ shows a spectral dependence, unlike ε_c. Table 2 displays the results of the sensitivity analysis.

References

Austin, R. (1974). Optical aspects of oceanography. *The remote sensing of spectral radiance from below the ocean surface* (pp. 317–344). London, UK: Academic Press Ch.

Bailey, S. W., & Werdell, P. J. (2006). A multi-sensor approach for the on-orbit validation of ocean color satellite data products. *Remote Sensing of Environment, 102*(1–2), 12–23.

Bates, J. S., Kelly, K. C., Johnson, J. E., & Gammon, R. H. (1995). Regional and seasonal variations in the flux of oceanic carbon monoxide to the atmosphere. *Journal of Geophysical Research, 100*(D11), 23093–23101.

Bélanger, S., Xie, H., Krotkov, N., Larouche, P., Vincent, W. F., & Babin, M. (2006). Photomineralization of terrigenous dissolved organic matter in arctic coastal waters from 1979 to 2003: Interannual variability and implications of climate change. *Global Biogeochemical Cycles, 20*, GB4005.

Berner, R. A., & Lasaga, A. C. (1989). Modeling the geochemical carbon cycle. *Scientific American*, 74–81.

Blough, N. V., & Del Vecchio, R. (2001). Biogeochemistry of marine dissolved organic matter. *Chromophoric DOM in the Coastal Environment* (pp. 509–546). San Diego: Academic Press Ch.

Bouillon, R. -C., & Miller, W. L. (2004). Determination of apparent quantum yield spectra of dms photo-degradation in an in situ iron-induced northeast Pacific Ocean bloom. *Geophysical Research Letters, 31*(6), 6310.

Bouillon, R. -C., & Miller, W. L. (2005). Photo-oxidation of DMS in natural waters: Laboratory assessment of the nitrate-photolysis induced DMS oxidation. *Environmental Science and Technology, 39*, 9471–9477.

Brimblecombe, P., & Shooter, D. (1986). Photooxidation of dimethylsulfide in aqueous solution. *Marine Chemistry, 19*, 343–353.

Conrad, R., Seiler, W., Bunse, G., & Giehl, H. (1982). Carbon monoxide in seawater (Atlantic Ocean). *Journal of Geophysical Research, 87*(C11), 8839–8852.

Cullen, J. J., Davis, R. F., Bartlett, J. S., & Miller, W. L. (1997). Toward remote sensing of UV attenuation, photochemical fluxes and biological effects in surface waters. *Proceedings of the 1997 Aquatic Sciences Meeting.* Santa Fe, NM, USA: ASLO.

Deal, C. J., Kieber, D. J., Toole, D. A., Stamnes, K., Jiang, S., & Uzuka, N. (2005). Dimethylsulfide photolysis rates and apparent quantum yields in Bering Sea seawater. *Continental Shelf Research, 25*(15), 1825–1835.

Eck, T. F., & Dye, D. G. (1991). Satellite estimation of incident photosynthetically active radiation using ultraviolet reflectance. *Remote Sensing of Environment, 38*(2), 135–146.

Eck, T. F., Bhartia, P. K., & Kerr, J. B. (1995). Satellite estimation of spectral UVB irradiance using TOMS derived total ozone and UV reflectivity. *Geophysical Research Letters, 22*, 611–614.

Erickson, D. J. (1989). Ocean to atmosphere carbon monoxide flux: Global inventory and climate implications. *Global Biogeochemical Cycles, 3*, 305–314.

Fichot, C., October 2004. Marine photochemistry from space. Master's thesis, Dalhousie University, Halifax, NS, Canada.

Fichot, C. G., Sathyendranath, S., & Miller, W. L. (2008). SeaUV and SeaUVc: Algorithms for the retrieval of UV diffuse attenuation coefficients from ocean color. *Remote Sensing of Environment, 112*(4), 1584–1602.

Gao, H., & Zepp, R. G. (1998). Factors influencing photoreactions of dissolved organic matter in a coastal river of the southeastern united states. *Environmental Science and Technology, 32*(19), 2940–2946.

Gordon, H. R., & McCluney, W. R. (1975). Estimation of the depth of sunlight penetration in the sea for remote sensing. *Applied Optics, 14*(2), 413–416.

Grant, R. H., & Gao, W. (2003). Diffuse fraction of UV radiation under partly cloudy skies as defined by the automated surface observation system (ASOS). *Journal of Geophysical Research (Atmospheres), 108*(D2), 4046.

Herman, J. R., & Celarier, E. A. (1997). Earth surface reflectivity climatology at 340–380 nm from TOMS data. *Journal of Geophysical Research, 102*, 28003–28012.

Huot, Y., Jeffrey, W. H., Davis, R. F., & Cullen, J. J. (2000). Damage to DNA in bacterioplankton: A model of damage by ultraviolet radiation and its repair as influenced by vertical mixing. *Photochemistry and Photobiology, 72*(1), 62–74.

IPCC. (2001). Climate change 2001: The scientific basis. Cambridge University Press.

Jin, Z., Charlock, T. P., & Rutledge, K. (2002). Analysis of broadband solar radiation and albedo over the ocean surface at cove. *Journal of Atmospheric and Oceanic Technology, 19*(10), 1585–1601.

Johannessen, S., 2000. A photochemical sink for dissolved organic carbon. Ph.D. thesis, Department of Oceanography, Dalhousie University, Halifax, NS, Canada, 171 pp.

Johannessen, S. C., & Miller, W. L. (2001). Quantum yield for the photochemical production of dissolved inorganic carbon in seawater. *Marine Chemistry, 76*(4), 271–283.

Johnson, E. A., August 2007. Investigating carbon monoxide (CO) consumption in the marine bacterium *Silibacter pomeroyi* (DSS3) with coxI gene expression. Master's thesis, University of Georgia.

Jones, R. D. (1991). Carbon monoxide and methane distribution and consumption in the photic zone of the sargasso sea. *Deep-Sea Research, 38*, 625–635.

Jones, R. D., & Morita, Y. (1983). Carbon monoxide oxidation by chemolithotrophic ammonium oxidizers. *Canadian Journal of Microbiology, 29*, 1545–1551.

Kara, A. B., Rochford, P. A., & Hurlburt, H. E. (2000). An optimal definition for ocean mixed layer depth. *Journal of Geophysical Research, 105*, 803.

Kara, A. B., Rochford, P. A., & Hurlburt, H. E. (2003). Mixed layer depth variability over the global ocean. *Journal of Geophysical Research*, 108(C3), 3079.

Kettle, A. J., 1994. A model of the temporal and spatial distribution of carbon monoxide in the mixed layer. Master's thesis, Massachusetts Institute of Technology/Woods Hole Oceanographic Institute.

Kettle, A. J. (2005). Diurnal cycling of carbon monoxide (CO) in the upper ocean near bermuda. *Ocean Modelling*, 8(4), 337–367.

Kieber, D. J., McDaniel, J. A., & Mopper, K. (1989). Photochemical source of biological substrates in seawater: Implications for geochemical carbon cycling. *Nature*, 341, 637–639.

Kieber, D. J., Jiao, J. F., Kiene, R. P., & Bates, T. S. (1996). Impact of dimethylsulfide photochemistry on methyl sulfur cycling in the equatorial Pacific Ocean. *Journal of Geophysical Research*, 101, 3715–3722.

Kirk, J. T. O. (1989). The upwelling light stream in natural waters. *Limnology and Oceanography*, 34(8), 1410–1425.

Kirk, J. T. O. (1994). Optics of UV-b radiation in natural waters. *Archiv für Hydrobiologie*, 43, 1–16.

Levitus, S., Boyer, T. P., 1994. World ocean atlas 1994, volume 4: Temperature. Tech. rep., NOAA Atlas NESDIS 4, National Oceanic and Atmospheric Administration, U.S. Department of Commerce, Washington, D.C.

Levitus, S., Burgett, R., Boyer, T. P., 1994. World ocean atlas 1994, volume 3: Salinity. Tech. rep., NOAA Atlas NESDIS 3, National Oceanic and Atmospheric Administration, U.S. Department of Commerce, Washington, D.C.

Loewus, M. W., & Delwiche, C. C. (1966). Carbon monoxide production by algae. *Plant Physiology*, 38, 371–374.

Miller, W. L. (1994). Aquatic and surface photochemistry. *Recent advances in the photochemistry of natural dissolved organic matter* (pp. 111–127). Boca Raton, FL: Lewis Publishers Ch.

Miller, G.W., 2000. Wavelength and temperature dependent quantum yields for photochemical formation of hydrogen peroxide in seawater. Master's thesis, State University of New York, College of Environmental Science and Forestry.

Miller, W. L., & Zepp, R. G. (1995). Photochemical production of dissolved inorganic carbon from terrestrial organic matter: Significance to the oceanic organic carbon cycle. *Geophysical Research Letters*, 22(4), 417–420.

Miller, W. L., Moran, M. A., Sheldon, W. M., Zepp, R. G., & Opsahl, S. (2002). Determination of apparent quantum yield spectra for the formation of biologically labile photoproducts. *Limnology and Oceanography*, 47(2), 343–352.

Mobley, C. D. (1994). *Light and water: Radiative transfer in natural waters.* New York: Academic Press.

Moore, R. M., & Zafiriou, O. C. (1994). Photochemical production of methyl iodide in seawater. *Journal of Geophysical Research*, 99, 16415–16420.

Mopper, K., & Kieber, D. J. (2000). The effects of UV radiation in the marine environment. *Marine photochemistry and its impact on carbon cycle* (pp. 101–129). New York, NY: Cambridge University Press Ch.

Mopper, K., & Kieber, D. J. (2001). Biogeochemistry of marine dissolved organic matter. *Photochemistry and cycling of carbon, sulfur, nitrogen and phosphorus* (pp. 456–509). San Diego: Academic Press Ch.

Mopper, K., Zhou, X., Kieber, R. J., Kieber, D. J., Sikorski, R. J., & Jones, R. D. (1991). Photochemical degradation of dissolved organic carbon and its impact on the oceanic carbon cycle. *Nature*, 353, 60–62.

Moran, M. A., & Miller, W. L. (2007). Resourceful heterotrophs make the most of light in the coastal ocean. *Nature Reviews Microbiology*, 5.

Neale, P. J., Brossard, P., Huot, Y., & Sommaruga, R. (2001). Incident and *in situ* irradiance in lakes Cadagno and Lucerne: A comparison of methods and models. *Aquatic Sciences*, 63, 250–264.

Nelson, N. A., & Siegel, D. A. (2001). Biogeochemistry of marine dissolved organic matter. *Chromophoric DOM in the open ocean* (pp. 547–579). San Diego: Academic Press Ch.

Nelson, N. B., Siegel, D. A., Carlson, C. A., Swan, C., Smethie, W. M., Jr., & Khatiwala, S. (2007). Hydrography of chromophoric dissolved organic matter in the North Atlantic. *Deep Sea Research Part I: Oceanographic Research Papers*, 54(5), 710–731.

NRL. (2006). *Naval research laboratory (nrl) mixed layer depth (nmld) climatology.*: U.S. Naval Research Laboratory, Stennis Space Center URL http://www7320.nrlssc.navy.mil/nmld/nmld.html

Ohta, K. (1997). Diurnal variations of carbon monoxide concentration in the equatorial pacific upwelling region. *Journal of Oceanography*, 53, 173–178.

Prieur, L., & Sathyendranath, S. (1981). An optical classification of coastal and oceanic waters based on the specific spectral absorption curves of phytoplankton pigments, dissolved organic matter, and other particulate materials. *Limnology and Oceanography*, 26(4), 671–689.

Remer, L. A., Kaufman, Y. J., Tanré, D., Mattoo, S., Chu, D. A., Martins, J. V., et al. (2005). The MODIS aerosol algorithm, products, and validation. *Journal of the Atmospheric Sciences*, 62(4), 947–973.

Ruggaber, R., Dlugi, R. A., & Nakajima, T. (1994). Modelling of radiation quantities and photolysis frequencies in the troposphere. *Journal of Atmospheric Chemistry*, 171–210.

Sarmiento, J. L. (1993). Ocean carbon cycle. *Chemical and Engineering News*, 30–43.

Seiler, W., & Junge, C. (1970). Carbon monoxide in the atmosphere. *Journal of Geophysical Research*, 75, 2217–2226.

Springer-Young, M. D., Erickson, D. J., & Carsey, T. P. (1996). Carbon monoxide gradients in the marine boundary layer of the North Atlantic Ocean. *Journal of Geophysical Research*, 101(D2), 4479–4484.

Stubbins, A., Uher, G., Kitidis, V., Law, C. S., Upstill-Goddard, R. C., Malcolm, E., et al. (2006). The open-ocean source of atmospheric carbon monoxide. *Deep Sea Research Part II: Topical Studies in Oceanography*, 53, 1685–1694.

Stubbins, A., Uher, G., Law, C. S., Mopper, K., Robinson, C., & Upstill-Goddard, R. C. (2006). Open-ocean carbon monoxide photoproduction. *Deep Sea Research Part II: Topical Studies in Oceanography*, 53, 1695–1705.

Stubbins, A., Hubbard, V., Uher, G., Law, C. S., Upstill-Goddard, R. C., Aiken, G. R., et al. (2008). Relating carbon monoxide photoproduction to dissolved organic matter functionality. *Environmental Science and Technology*, 42(9), 3271–3276.

Swinnerton, J. W., Linnenbom, V. J., & Lamontagne, R. A. (1970). The ocean: A natural source of carbon monoxide. *Science*, 167, 984–986.

Tolli, J. D., Sievert, S. M., & Taylor, C. D. (2006). Unexpected Diversity of Bacteria Capable of Carbon Monoxide Oxidation in a Coastal Marine Environment, and Contribution of the Roseobacter-Associated Clade to Total CO Oxidation. *Applied and Environmental Microbiology*, 72(3), 1966–1973.

Uher, G., & Andreae, M. O. (1997). Photochemical production of carbonyl sulfide in North Sea water: A process study. *Limnology and Oceanography*, 42, 432–442.

Vähätalo, A. V., Salkinoja-Salonen, M., Taalas, P., & Salonen, K. (2000). Spectrum of the quantum yield for photochemical mineralization of dissolved organic carbon in a humic lake. *Limnology and Oceanography*, 45(3), 664–676.

Valentine, R. L., & Zepp, R. G. (1993). Formation of carbon monoxide from the photodegradation of terrestrial dissolved organic carbon in natural waters. *Environmental Science and Technology*, 27, 409–412.

Xie, H., & Gosselin, M. (2005). Photoproduction of carbon monoxide in first-year sea ice in Franklin Bay, southeastern Beaufort Sea. *Geophysical Research Letters*, 32, L12606.

Xie, H., Moore, R. M., & Miller, W. L. (1998). Photochemical production of carbon disulfide in seawater. *Journal of Geophysical Research*, 103(C3), 5331–5644.

Xie, H. X., Zafiriou, O. C., Umile, T. P., & Kieber, D. J. (2005). Biological consumption of carbon monoxide in Delaware Bay, NW Atlantic and Beaufort Sea. *Marine Ecology Progress Series*, 290, 1–14.

Yamashita, Y., & Tanoue, E. (2009). Basin scale distribution of chromophoric dissolved organic matter in the Pacific Ocean. *Limnology and Oceanography*, 54(2), 598–609.

Zafiriou, O. C., Andrews, S. S., & Wang, W. (2003). Concordant estimates of oceanic carbon monoxide source and sink processes in the pacific yield a balanced global "blue-water" co budget. *Global Biogechemical Cycles*, 17(01), 1015–1027.

Zafiriou, O. C., Xie, H., Nelson, N. B., Najjar, R. G., & Wang, W. (2008). Diel carbon monoxide cycling in the upper Sargasso Sea near Bermuda at the onset of spring and in midsummer. *Limnology and Oceanography*, 53(2), 835–850.

Zepp, R. G., Callaghan, T. V., & Erickson, D. J. (1998). Effects of enhanced solar ultraviolet radiation on biogeochemical cycles. *Journal of Photochemistry and Photobiology*, 46, 69–82.

Zepp, R. G., Erickson-III, D. J., Paul, N. D., & Sulzberger, B. (2007). Interactive effects of solar uv radiation and climate change on biogeochemical cycling. *Photochemical and Photobiological Sciences*, 6, 286–300.

Zhang, Y., Chen, G., & Xie, H. (2006). Factors affecting the efficiency of carbon monoxide photoproduction in the St. Lawrence estuarine system (Canada). *Environmental Science and Technology*, 40(24), 7771–7777.

Zhang, Y., Xie, H., Fichot, C. G., & Chen, G. (2008). Dark production of carbon monoxide (co) from dissolved organic matter in the St. Lawrence estuarine system: Implication for the global coastal and blue water co budgets. *Journal of Geophysical Research*, 113(C12020).

Zheng, X., Dickey, T., & Chang, G. (2002). Variability of the downwelling diffuse attenuation coefficient with consideration of inelastic scattering. *Applied Optics*, 41(30), 6477–6488.

Ziolkowski, L. A., & Miller, W. L. (2007). Variability of the apparent quantum efficiency of co photoproduction in the Gulf of Maine and Northwest Atlantic. *Marine Chemistry*, 105, 258–270.

Zuo, Y., & Jones, R. D. (1995). Formation of carbon monoxide by photolysis of dissolved organic material and its significance in the carbon cycling of the oceans. *Naturwissenschaften*, 82(10), 472–474.